NASA TECHNICAL NOTE

NASA TN D-5940

FIXED-BASE VISUAL SIMULATION OF OBSTACLE AVOIDANCE DURING TERMINAL DESCENT OF ADVANCED APOLLO SPACECRAFT WITH AN ALL-FLEXIBLE PARAWING

by G. Kimball Miller, Jr.

Langley Research Center
Hampton, Va. 23365

NATIONAL AERONAUTICS AND SPACE ADMINISTRATION • WASHINGTON, D. C. • AUGUST 1970

0132725

1. Report No. NASA TN D-5940	2. Government Accession No.	3. Recipient's Catalog No.
4. Title and Subtitle FIXED-BASE VISUAL SIMULATION OF OBSTACLE AVOIDANCE DURING TERMINAL DESCENT OF ADVANCED APOLLO SPACECRAFT WITH AN ALL-FLEXIBLE PARAWING		5. Report Date August 1970
		6. Performing Organization Code
7. Author(s) G. Kimball Miller, Jr.		8. Performing Organization Report No. L-7116
9. Performing Organization Name and Address NASA Langley Research Center Hampton, Va. 23365		10. Work Unit No. 125-19-11-05
		11. Contract or Grant No.
12. Sponsoring Agency Name and Address National Aeronautics and Space Administration Washington, D.C. 20546		13. Type of Report and Period Covered Technical Note
		14. Sponsoring Agency Code

15. Supplementary Notes

16. Abstract

A fixed-base visual simulation study has been conducted to determine the ability of an onboard pilot to control a single-keel all-flexible parawing and advanced Apollo spacecraft combination so as to avoid obstacles located in the desired landing area. The results of the investigation showed that the pilot avoided the obstacles approximately 96 percent of the flights and generally landed within 500 ft (152.4 m) of the center of the desired site regardless of the maximum turn-rate capability of the vehicle.

17. Key Words (Suggested by Author(s)) Descent systems Land landings Parawings Obstacle avoidance	18. Distribution Statement Unclassified — Unlimited		
19. Security Classif. (of this report) Unclassified	20. Security Classif. (of this page) Unclassified	21. No. of Pages 49	22. Price* $3.00

*For sale by the Clearinghouse for Federal Scientific and Technical Information
Springfield, Virginia 22151

FIXED-BASE VISUAL SIMULATION OF OBSTACLE AVOIDANCE

DURING TERMINAL DESCENT OF ADVANCED APOLLO SPACECRAFT

WITH AN ALL-FLEXIBLE PARAWING

By G. Kimball Miller, Jr.
Langley Research Center

SUMMARY

A fixed-base visual simulation study using wind-tunnel aerodynamics has been conducted to determine the ability of an onboard pilot to control a single-keel all-flexible parawing and an advanced Apollo spacecraft combination so as to avoid obstacles in the desired landing area. In the investigation, a closed-circuit television system in conjunction with an earth-terrain model was employed for image generation, and six rigid-body degrees of freedom of the vehicle were simulated. The pilot controlled the vehicle through a single-axis hand controller which activated constant-rate reels to induce differential changes in the wing-tip lines for lateral control. Longitudinal and lateral trim controls could be commanded through a thumb switch on the hand controller. The simulated viewing system provided the pilot with a field of view of 34.6^O vertical by 48.3^O horizontal. The pilot's task was to assume control of the vehicle under the influence of winds with maximum velocities up to 26 ft-sec^{-1} (7.9 m-sec^{-1}) at initial altitudes up to 2000 ft (609.6 m) and land as close as possible to the center of a specified landing site with the vehicle headed into the wind to reduce ground speed from 29 ft-sec^{-1} (8.8 m-sec^{-1}) experienced in still air.

The results of the investigation showed that the pilot avoided the obstacles 95.5 percent of the flights and landed with a heading error of 10° or less 59 percent of the flights with a miss distance generally less than 500 ft (152.4 m). Increasing the vehicle turn-rate capability by a factor of about 3 had little effect on terminal accuracy and resulted in a tendency of the pilot to overcontrol when the higher turn rates were used.

INTRODUCTION

Spacecraft recovery systems which employ all-flexible parawings to provide accurate terminal control and low horizontal and vertical velocities at touchdown are currently of interest. The ability of an onboard pilot to control an all-flexible parawing and advanced Apollo spacecraft combination at initial altitudes up to 18 000 ft (5486.4 m) so

as to attain specified landing sites was demonstrated in a simulation study reported in reference 1. The reference indicated that a maximum turn-rate capability of approximately 9° sec^{-1} was satisfactory and that the pilots could consistently attain the desired landing site under various wind conditions. Although these low turn rates are generally satisfactory in descending flight, they may not be satisfactory for low-altitude obstacle avoidance.

The present fixed-base simulator study was performed to determine the ability of an onboard pilot to control an all-flexible parawing and advanced Apollo spacecraft combination so as to avoid obstacles with near-zero vertical dimension, such as rivers, gullies, and fences, which are representative of those present in contemplated landing areas for this type of descent system. The flights were initiated at an altitude of approximately 2000 ft (609.6 m) with wind velocities from 0 to 26 ft-sec^{-1} (7.9 m-sec^{-1}) and various wind directions. The investigation employed the 1962 U.S. Standard Atmosphere.

Pilots seated in the Apollo spacecraft cannot see the ground when the vehicle is suspended with the heat shield down. Consequently, an onboard viewing system was included which had a field of view of 34.6° vertical by 48.3° horizontal and could be controlled in pitch by the pilot. The pilot had a view from the local vertical forward 34.6° when the viewing system was directed in its maximum downward position. In its maximum upward position, the pilot had a view of $\pm 17.3^{\circ}$ about the earth's horizon.

Equations of motion permitting six rigid-body degrees of freedom were used to represent the vehicle and were solved in real time by a digital computer. The pilot controlled the vehicle through a single-axis hand controller. The inputs from the hand controller actuated constant-rate reels which changed the right and left parawing-tip lines for lateral control.

<div align="center">EQUATIONS OF MOTION</div>

Measurements for this investigation were made in U.S. Customary Units but are also given in the International System of Units (SI). (See ref. 2.) The symbols used in the present study are presented in appendix A. The equations of motion which permitted six rigid-body degrees of freedom of the vehicle and the transformation matrices for the assumed axis systems are presented in appendix B. The rigid-body assumptions were made on the basis of observations of wind-tunnel models and flight-test models which indicated that the parawing and the payload are tightly coupled in fully deployed gliding flight. The form of the equations of motion was dictated by the requirements of the simulation equipment used in the study. The force equations were written with respect to cylindrical coordinates and the moment equations with respect to body axes.

To permit the simulation of several different configurations without extensive reprograming for each configuration, the computer program used in the present investigation included the equations (appendix C) required to transfer the basic aerodynamic derivatives of the parawing from the confluence of the suspension lines to the center of gravity of the parawing-payload combination. The equations added to the flexibility of the program in that simulated configurations could be completely changed merely by changing a few constants.

VEHICLE DESCRIPTION

The simulated configuration consisted of a single-keel 45° all-flexible parawing with a one-eighth keel-length nose cut and an advanced Apollo spacecraft suspended as indicated in figure 1. The simulated all-flexible parawing was geometrically similar to that described in reference 3, including the number and placement of the suspension lines. The wing loading of the vehicle (parawing-payload combination) was 1.28 lb-ft^{-2} (61.28 N-m^{-2}). The wing material was assumed to have a weight of 2.2 oz-yd^{-2} (0.075 kg-m^{-2}) and the suspension lines had a weight of 128 lb (58.06 kg). Pertinent characteristics of the wing when flat were

$$l_k = 131.8 \text{ ft} \quad (40.2 \text{ m})$$

$$b = 186.2 \text{ ft} \quad (56.7 \text{ m})$$

$$S = 12\ 000 \text{ ft}^2 \quad (1114.8 \text{ m}^2)$$

The moments of inertia of the 15 000-lb (6804 kg) payload were

$$I_{XP} = 7300 \text{ slug-ft}^2 \quad (9897.3 \text{ kg-m}^2)$$

$$I_{YP} = 6456 \text{ slug-ft}^2 \quad (8753.0 \text{ kg-m}^2)$$

$$I_{ZP} = 5858 \text{ slug-ft}^2 \quad (7942.3 \text{ kg-m}^2)$$

The cross products of inertia were assumed to be negligible and were omitted.

The mass and inertia of a parawing is greater in air than in a vacuum because of the air trapped within the canopy envelope and because some of the surrounding air is also set in motion. The inertia of a 24-ft (7.3 m) keel parawing has been determined experimentally (ref. 4) and includes apparent mass and inertia effects. The inertias of

the wing and suspension lines, including apparent inertia effects, for the 131.8-ft (40.2 m) keel parawing used in the present simulation were estimated from the small scale data of reference 4 and are presented in figure 2. The apparent-mass effects were generally assumed to be zero in the present study. The parawing inertias (fig. 2) and the payload inertias were combined to give the total inertias of the vehicle by using the equations presented in appendix C.

During descent under the inflated parawing, the heat shield was down and the astronaut's view through the advanced Apollo windows was upward in the direction of the wing. It was, therefore, necessary to include an auxiliary viewing system that would enable the pilot to view the earth. The viewing system used in the simulation had a field of view of 34.6^O vertical by 48.3^O horizontal. The direction of the optical axis of the viewing system could be controlled by the pilot to any angular position between the Apollo X-axis and a point approximately 75° below the X-axis.

Because longitudinal control was quite small and thus of little practical use (ref. 1), only a single-axis hand controller was employed which provided lateral control by actuating simulated constant-rate $\left(0.02l_k \text{ sec}^{-1}\right)$ reels to deflect differentially the right and left wing-tip lines. A four-position thumb switch on the hand controller was used to trim the vehicle both longitudinally (by deflecting the rear keel line) and laterally (by differential wing-tip deflection).

SIMULATION EQUIPMENT

The equipment used in the simulation is depicted in figure 3. A fixed-base cockpit (fig. 4) was fitted with a television monitor that provided a field of view of 34.6^O vertical by 48.3^O horizontal to the pilot. The instruments used during the flights were the three-axis gyro horizon, the altimeter, and the control line position indicators. The remaining instruments were used only for checkout purposes. A single-axis hand controller with a dead band that was 25 percent of maximum deflection in roll was located to the right of the pilot's seat. Depressing the trigger and deflecting the control stick activated constant-rate reels to drive the right and left wing-tip lines differentially. When the controller was returned to the neutral position with the trigger depressed, the control lines remained at their given position. The control lines could be returned to the trim position by releasing the trigger with the control stick in any position. Lateral and longitudinal trim inputs activated the wing-tip-line reels and rear-keel-line reel, respectively, at $0.01l_k \text{ sec}^{-1}$. Control inputs were transmitted to a digital computer which solved the equations of motion in real time and generated drive signals for the simulation equipment.

The visual presentation was obtained by means of an 875-scan-line image orthicon television camera in conjunction with an optical pickup similar to that described in reference 5. The optical pickup was driven by the output of the moment equations to provide the three rotational degrees of freedom of the vehicle. The three translational degrees of freedom were obtained by mounting the optical pickup and camera combination on a transport system that moved relative to a terrain model in response to the output of the force equations. The earth-terrain model was a 22.0- by 34.9-ft (6.7 by 10.6 m) translucent back-lighted screen, scaled at 1200:1, and was an adaptation of part of a Langley Research Center simulator originally designed to study lunar operations. A transparent photograph of an artist's concept of the Wallops Island, Virginia, runway complex, representing an area approximately 12 000 ft (3657.6 m) square, was mounted on the front of the model (fig. 5). In addition, 20 appropriately scaled buildings were placed on the transparency. It should be noted that model protection considerations imposed a minimum altitude limit of approximately 30 ft (9.1 m), at which altitude an electrical stop was activated.

AERODYNAMIC PARAMETERS

The aerodynamic and control parameters employed in the present investigation are the same as those used in the study in reference 1 and do not include the payload aerodynamics. All parameters are based on the span and area of the parawing when flat and are referenced to the system of reference axes (fig. 1) located at the theoretical confluence of the suspension lines.

The aerodynamic data were programed on a digital computer in the straight-line segments shown in figure 6. The computer program transferred the data to the center of gravity of the parawing-payload combination by means of the equations presented in appendix C. The data in figures 6(a) and 6(c) were obtained from the static wind-tunnel measurements of an 18-ft (5.5 m) keel model presented in reference 3.

The sideslip and dynamic derivatives in figure 6(b) were obtained from forced oscillation tests of a 5-ft (1.5 m) keel model in the Langley full-scale tunnel. The small model was used because of its adaptability to existing test equipment. It should be noted that the oscillatory test technique used to obtain these data yields combination derivatives in which the acceleration terms appear. Thus, the derivatives in figure 6(b) are combination derivatives $\left(\text{of the form} \quad C_{l_p} + C_{l_{\dot{\beta}}} \sin \alpha\right)$ and were obtained from measurements of the force and moment components in phase and out of phase with the model motion. Since measurements of the acceleration derivatives do not exist at present, separation of the combination derivatives was impossible. Reference 6, however, indicates that the aerodynamic effect of the acceleration derivatives for rigid leading-edge conical

5

parawings appears to be negligible in the angle-of-attack range below the stall. Therefore, the oscillation test data were assumed to be simply those noted in figure 6(b), that is, the combination $C_{l_p} + C_{l_{\dot{\beta}}} \sin \alpha$ was assumed to be C_{l_p}, and so forth.

TASK DESCRIPTION

The flights originated at altitudes up to 2000 ft (609.6 m) with the vehicle upwind of a designated landing site and generally headed into the wind. The pilot's task was to control the vehicle so as to attain the center of the designated landing site with the vehicle heading into the wind at flight termination (30-ft (9.1 m) altitude) to reduce ground speed. The primary landing site used in the present study was the 500-ft by 700-ft by 750-ft grassy triangle (152.4 m by 213.4 m by 228.6 m) formed by three intersecting runways (fig. 7). The minimum turn radius of the advanced Apollo and parawing combination was approximately 225 ft (68.6 m) (ref. 1). A circle of this minimum turn radius can not be accomplished within the boundary of the primary landing site (fig. 7). Because the vehicle was not capable of turning 360° inside the triangle, the acceptable landing area included the three grassy plots adjacent to the triangle. The runways separating these four grassy plots constituted obstacles to be avoided. These two-dimensional obstacles were believed to be representative because the landing areas contemplated for the advanced Apollo and parawing descent systems contain obstacles with a near-zero vertical dimension; that is, the landing area will probably contain gullies, streams, or fences, but will not contain forrests or high buildings near the primary landing site.

Four wind profiles (fig. 8), scaled in decreasing magnitude from A to D, were used in the investigation. The wind magnitudes ranged from very nearly zero for wind D at low altitude to approximately the still air forward speed of the vehicle (29 ft-sec^{-1} (8.8 m-sec^{-1})) for wind A at flight initiation. For a given wind profile, the flight initiation point was always chosen so that the primary landing site could be attained with proper maneuvering. In all flights, the terminal magnitude and direction of the wind were known by the pilot.

RESULTS AND DISCUSSION

The results presented herein were obtained by a pilot (research engineer) who was considered to be well trained inasmuch as he had participated in the simulation study reported in reference 1 and in several radio-controlled flight tests of small-scale parawings.

6

Preliminary Results

Although 131.8-ft (40.2 m) keel parawings have not been flight tested at the present time, a 24-ft (7.3 m) keel parawing has undergone preliminary flight tests. Therefore, to provide a comparison between simulator results and flight-test results, a parawing with a 24-ft-long (7.3 m) keel and a wing loading of 1.15 lb-ft^{-2} (55.06 N-m^{-2}) was simulated by using the aerodynamic parameters presented in figure 6. At the present time flight-test data at a wing loading of 1.15 lb-ft^{-2} (55.06 N-m^{-2}) are not available. Consequently, the flight-test data presented herein for a wing loading of 1.15 lb-ft^{-2} (55.06 N-m^{-2}) were interpolated from flight-test data obtained at the Langley Research Center at wing loadings of 0.394, 0.700, 1.000, and 1.300 lb-ft^{-2} (18.86, 33.51, 47.87, and 62.24 N-m^{-2}). There is good agreement (fig. 9(a)) between turn rates (obtained by timing 360° turns) experienced during flight tests and those generated on the simulator for lateral control inputs up to $0.033 l_k$, the maximum input employed with the small-scale parawing. In addition, the increase in rate of descent with an increase in turn rate obtained by simulation (fig. 9(b)) agrees reasonably well with the flight-test data. It thus appears that the aerodynamic parameters used in the simulation are representative of those for all-flexible parawings.

Apparent Mass and Inertia Effects

In addition to the 131.8-ft (40.2 m) keel parawing with moments of inertia given in figure 2 and zero apparent mass, two other configurations were simulated to examine the effects of apparent mass and inertia variations on pilot performance. The second configuration arbitrarily included an apparent mass of approximately 250 slugs (3648.5 kg) with no inertia changes, whereas the third configuration employed zero apparent mass and moments of inertia that were reduced from those of figure 2 by approximately 10 percent for I_{XW}, 20 percent for I_{YW}, and 75 percent for I_{ZW}. Time histories of a specific maneuver with each of the three configurations are shown in figure 10. The pilot was unable to detect the differences in the flight characteristics of the three configurations in figure 10. However, the vehicle turn rate for a given lateral control input was somewhat less for these three configurations than it was for the vehicle with zero apparent mass and inertia reported in reference 1. For example, a control input $\Delta L_C / l_k$ of 0.04 resulted in an approximately 4° sec^{-1} turn rate for the three configurations of figure 10, whereas the vehicle in reference 1 was capable of a 5.5° sec^{-1} turn rate when the apparent mass and inertia were omitted.

Piloting Techniques

Ground tracks of representative flights made under the influence of the four wind profiles used during the study are presented in figure 11. The flight techniques used

by the pilot were generally the same as those given in reference 1. In the higher velocity winds A, B, and C, the pilot generally controlled the vehicle to some point downwind of the landing site, turned into the wind to land, and performed S-turns to lose altitude if it appeared the vehicle was going to overshoot the center of the landing site. The use of S-turns to lose altitude near the landing site was ineffective in low winds because the ground speed was relatively high and resulted in the vehicle moving farther away from the landing site than the pilot desired. Consequently, for wind D the pilot generally remained outside the boundaries of the primary landing site; he kept the landing site in view until altitude was reduced so that he could turn and run straight toward the center of the target for touchdown. Occasionally, during the final approach, the pilot could not attain the primary landing site and it was necessary to land in one of the three alternate areas. Time histories of typical flights made in a low wind (wind D) and a high wind (wind A) are shown in figures 12 and 13, respectively.

Terminal Accuracy

The primary concern of the present investigation was to determine the ability of a pilot to avoid obstacles that might be located in the desired landing area. Approximately 200 flights were made under the influence of various wind conditions (fig. 8). The pilot was able to avoid the obstacles (runways) 95.5 percent of the flights (table I) and had a terminal heading error of less than 10° (which was believed to be a reasonable allowable error) approximately 59.0 percent of the flights. The pilot performed emergency landings in one of the three alternate sites 11.4 percent of the flights.

TABLE I.- TERMINAL ACCURACY

Wind profile	Number of simulator runs	Miss distance, ft (m)		Heading error, $\Delta\lambda$, deg		Percent of runs with heading error $\leq 10^{\circ}$	Percent of runs	
		Arithmetic mean	Standard deviation	Arithmetic mean	Standard deviation		Avoided obstacles	Emergency alternate
A	56	191.7 (58.4)	164.4 (50.1)	-3.3	19.7	51.8	94.7	8.9
B	58	194.6 (59.3)	145.5 (44.3)	-1.2	18.0	60.3	94.8	13.8
C	31	169.7 (51.7)	155.2 (47.3)	-4.8	22.4	71.0	100.0	6.4
D	56	338.4 (103.1)	205.9 (62.7)	Not applicable	Not applicable	Not applicable	96.5	16.1
All flights	201	229.9 (70.1)	182.2 (55.5)	-2.9	20.3	59.0	95.5	11.4

Because little reduction in ground speed could be achieved by heading into the wind for low wind D, the pilot ignored his heading angle at flight termination and concentrated on landing as close as possible to the center of the landing site. Even though the pilot was able to concentrate more heavily on attaining small miss distances, the terminal accuracy experienced with wind D was considerably poorer than that with higher winds because the relatively high ground speed resulted in a tendency to overshoot the desired landing site.

In this investigation, the miss distances were considerably smaller than those of the simulation in reference 1 for which the mean miss distance was 618.6 ft (188.5 m) with a standard deviation of 446.4 ft (136.1 m). The landing area used in reference 1 had no recognizable landmarks near the primary landing site and the pilots frequently became disoriented at low altitudes. In the present study the pilot was able to compensate for the small field of view and obtain smaller miss distances by using the known pattern of the runway area as orientation cues relative to the primary landing site. During low-altitude maneuvers, the primary landing site was outside the small-angle field of view for extended periods of time. However, with a well-defined pattern of readily recognizable landmarks surrounding the primary landing site, the pilot was always able to remain properly oriented.

Supplementary Investigation

It was believed that a vehicle with a high-turn-rate capability (that is, which could turn inside the boundaries of the primary landing site) would make the obstacle avoidance task considerably easier. A turn-rate capability of approximately 25° $\sec^{-1}$ was obtained by simulating the 24-ft (7.3 m) keel parawing and using the aerodynamics parameters presented in figure 6.

TABLE II.- TERMINAL ACCURACY (HIGH-TURN-RATE CAPABILITY)

Wind profile	Number of simulator runs	Miss distance, ft (m)				Heading error, $\Delta\lambda$, deg		Percent of runs with heading error $\leq 10^{\circ}$	Percent of runs	
		Arithmetic mean		Standard deviation		Arithmetic mean	Standard deviation		Avoided obstacles	Emergency alternate
A	40	160.9	(49.04)	126.5	(38.6)	-0.6	31.9	47.5	100.0	7.5
B	40	142.8	(43.5)	131.0	(39.9)	-8.7	25.3	55.0	92.5	7.5
C	41	131.7	(40.1)	112.1	(34.2)	.9	18.8	65.8	95.1	4.9
D	40	233.6	(71.2)	146.6	(44.7)	Not applicable	Not applicable	Not applicable	100.0	2.5
All flights	161	167.0	(50.9)	133.9	(40.8)	-2.7	26.0	57.9	96.9	5.0

The terminal accuracy that the pilot was able to attain with the high-turn-rate capability is shown in table II for the four wind profiles used in the present study. The pilot's ability to avoid obstacles with the vehicle having a high-turn-rate capability was only slightly improved (96.9 percent successful) over that with the full-scale vehicle having a low-turn-rate capability (95.5 percent successful). It was not necessary, however, for the pilot to perform emergency landings in the alternate sites as frequently with the high-turn-rate vehicle, which resulted in smaller miss distances particularly for flights made under the influence of low wind D. The terminal heading error increased somewhat with high turn rates, primarily because of a tendency to overcontrol. To minimize the overcontrol problem that existed when high turn rates were employed, the pilot generally

planned the flights with turn rates of approximately 8° sec^{-1} and used the higher turn rates only in the event of an emergency.

CONCLUDING REMARKS

A fixed-base visual simulation study has been conducted to determine the ability of an onboard pilot to control a 131.8-ft (40.2 m) keel all-flexible parawing and advanced Apollo spacecraft combination so as to avoid obstacles located in the desired landing area. The investigation included six rigid-body degrees of freedom of the vehicle. The pilot's task was to control the vehicle, under the influence of winds with maximum veloc- ities up to 26 ft-sec^{-1} (7.9 m-sec^{-1}), at initial altitudes up to 2000 ft (609.6 m) and land as close as possible to the center of a specified landing site with the vehicle headed into the wind to reduce ground speed.

Within the limits of the simulation, the results of the study showed that the pilot could avoid obstacles with near-zero vertical dimension, such as rivers, gullies, and fences, 95.5 percent of the flights and land with a heading error of 10° or less approxi- mately 59 percent of the flights. A landing area that included a readily recognizable pat- tern of landmarks in the vicinity of the primary landing site provided orientation cues which were useful during low-altitude maneuvers when the primary landing site was out- side the pilot's narrow field of view. These orientation cues permitted the pilot to reduce the miss distances to less than one-half those experienced in the investigation of NASA TN D-5049 for which orientation cues were not available.

To compare the simulated and flight-test vehicle characteristics, a 24-ft (7.3 m) keel vehicle was also simulated. The turn-rate capability of the small-scale vehicle was approximately three times that of the full-scale vehicle and the simulated turn rates agreed very well with flight-test results up to about 25° sec^{-1}. However, very little improvement in the pilot's ability to avoid obstacles and attain small miss distances was experienced by using high turn rates. The pilot generally planned the flights with turn rates of about 8° sec^{-1} and used the higher turn rates only in the event of an emergency. The pilot was unable to detect changes in vehicle performance due to inertia variations of approximately 10, 20, and 75 percent in roll, pitch, and yaw, respectively.

Langley Research Center,
National Aeronautics and Space Administration,
Hampton, Va., April 30, 1970.

APPENDIX A

SYMBOLS

The assumed axis systems are shown in figure 14.

A_{ij} direction cosines, where $i = 1, 2, 3$ and $j = 1, 2, 3$

b span of flexible parawing when flat, feet (meters)

$$C_l = \frac{\text{Rolling moment about } X_R\text{-axis}}{QSb}$$

$$C_m = \frac{\text{Pitching moment about } Y_R\text{-axis}}{QSb}$$

$$C_n = \frac{\text{Yawing moment about } Z_R\text{-axis}}{QSb}$$

$$C_X = \frac{\text{Force along } X_R\text{-axis}}{QS}$$

$$C_Y = \frac{\text{Force along } Y_R\text{-axis}}{QS}$$

$$C_Z = \frac{\text{Force along } Z_R\text{-axis}}{QS}$$

$C_{m,0}$ value of C_m at zero angle of attack

$C_{X,0}$ value of C_X at zero angle of attack

$C_{Z,0}$ value of C_Z at zero angle of attack

$$C_{m_\alpha} = \frac{\partial C_m}{\partial \alpha}, \text{ per radian}$$

$$C_{X_\alpha} = \frac{\partial C_X}{\partial \alpha}, \text{ per radian}$$

11

$$C_{Z_\alpha} = \frac{\partial C_Z}{\partial \alpha}, \text{ per radian}$$

$$C_{l_\beta} = \frac{\partial C_l}{\partial \beta}, \text{ per radian}$$

$$C_{n_\beta} = \frac{\partial C_n}{\partial \beta}, \text{ per radian}$$

$$C_{Y_\beta} = \frac{\partial C_Y}{\partial \beta}, \text{ per radian}$$

$$C_{l_p} = \frac{\partial C_l}{\partial \frac{pb}{2V_R}}, \text{ per radian}$$

$$C_{n_p} = \frac{\partial C_n}{\partial \frac{pb}{2V_R}}, \text{ per radian}$$

$$C_{Y_p} = \frac{\partial C_Y}{\partial \frac{pb}{2V_R}}, \text{ per radian}$$

$$C_{m_q} = \frac{\partial C_m}{\partial \frac{qb}{2V_R}}, \text{ per radian}$$

$$C_{X_q} = \frac{\partial C_X}{\partial \frac{qb}{2V_R}}, \text{ per radian}$$

$$C_{Z_q} = \frac{\partial C_Z}{\partial \frac{qb}{2V_R}}, \text{ per radian}$$

$$C_{l_r} = \frac{\partial C_l}{\partial \frac{rb}{2V_R}}, \text{ per radian}$$

$$C_{n_r} = \frac{\partial C_n}{\partial \frac{rb}{2V_R}}, \text{ per radian}$$

$$C_{Y_r} = \frac{\partial C_Y}{\partial \frac{rb}{2V_R}}, \text{ per radian}$$

$\dfrac{\partial C_X}{\partial \left|\frac{\Delta L}{l_k}\right|}, \dfrac{\partial C_Z}{\partial \left|\frac{\Delta L}{l_k}\right|}, \dfrac{\partial C_m}{\partial \left|\frac{\Delta L}{l_k}\right|}$ variation in C_X, C_Z, and C_m, respectively, due to lateral inputs

$\dfrac{\partial C_{Y_\beta}}{\partial \left|\frac{\Delta L}{l_k}\right|}, \dfrac{\partial C_{n_\beta}}{\partial \left|\frac{\Delta L}{l_k}\right|}, \dfrac{\partial C_{l_\beta}}{\partial \left|\frac{\Delta L}{l_k}\right|}$ variation in C_{Y_β}, C_{n_β}, and C_{l_β}, respectively, due to lateral inputs

$\dfrac{\partial C_X}{\partial \frac{\Delta l}{l_k}}, \dfrac{\partial C_Z}{\partial \frac{\Delta l}{l_k}}, \dfrac{\partial C_m}{\partial \frac{\Delta l}{l_k}}$ trim control parameters (that is, changes in coefficients due to longitudinal trim inputs)

$\dfrac{\partial C_Y}{\partial \frac{\Delta L}{l_k}}, \dfrac{\partial C_n}{\partial \frac{\Delta L}{l_k}}, \dfrac{\partial C_l}{\partial \frac{\Delta L}{l_k}}$ lateral control parameters (that is, changes in coefficients due to lateral inputs)

c, d, e, f quaternions or Euler parameters (ref. 7)

F_{XB}, F_{YB}, F_{ZB} aerodynamic force along X_B-, Y_B-, and Z_B-axis, respectively, pounds (newtons)

g_e acceleration at surface of earth due to gravitational attraction, 32.2 feet-second^{-2} (9.81 meters-second^{-2})

13

h   altitude above surface of earth, feet (meters)

I_{XB}, I_{YB}, I_{ZB} moments of inertia of parawing-payload combination including apparent inertias, slug-feet^2 (kilogram-meters^2)

I_{XP}, I_{YP}, I_{ZP} moments of inertia of payload, slug-feet^2 (kilogram-meters^2)

I_{XW}, I_{YW}, I_{ZW} moments of inertia of the parawing and suspension lines including apparent inertias, slug-feet^2 (kilogram-meters^2)

ΔL sum of lateral control and trim inputs (that is, differential deflection of right and left wing-tip lines where right roll is obtained by shortening right and lengthening left tip lines (positive ΔL)), feet (meters)

ΔL_C lateral control input, feet (meters)

ΔL_T lateral trim input, feet (meters)

l_k parawing keel length when flat, feet (meters)

Δl longitudinal trim input (that is, change in rear-keel-line length from that required for trim at $\alpha = 30^\circ$), feet (meters)

M_{XB}, M_{YB}, M_{ZB} aerodynamic moment about X_B-, Y_B-, and Z_B-axis, respectively, foot-pounds (meter-newtons)

m_a apparent mass, slugs (kilograms)

m_B mass of parawing-payload combination excluding apparent mass, slugs (kilograms)

m_P mass of payload, slugs (kilograms)

m_W mass of parawing and suspension lines excluding apparent mass, slugs (kilograms)

p, q, r vehicle angular velocity about X_B-, Y_B-, and Z_B-axis, respectively, radians/second or degrees/second

Q   dynamic pressure, pounds-foot^{-2} (newtons-meter^{-2})

R, Ψ, Y   cylindrical coordinate system with origin at center of earth and vector R and angle Ψ in XZ-plane (see fig. 14)

R_e assumed radius of earth, 20.9×10^6 feet (6.37×10^6 meters)

S   area of parawing when flat, feet^2 (meters^2)

t   time, seconds

V_R relative wind velocity, feet-second^{-1} (meters-second^{-1})

V_{XY} velocity in plane parallel to surface of earth (ground speed), feet-second^{-1} (meters-second^{-1})

X, Y, Z   fixed-reference axis system with origin at center of earth which was assumed to be a nonrotating homogeneous sphere (see fig. 14)

X_B, Y_B, Z_B vehicle body axis system with origin at center of gravity of parawing-payload combination (see fig. 14)

X_C, Y_C, Z_C moving-reference axis system with origin at surface of earth and with Z_C-axis alined with local vertical and positive inward, X_C-axis positive westward, and Y_C-axis positive northward (see fig. 14)

X_O, Y_O, Z_O optical axis system with origin at center of gravity of vehicle (differs from body axes by angle θ_O) (see fig. 14)

X_P, Y_P, Z_P axis system with origin at center of gravity of payload and parallel to vehicle body axis system

X_R, Y_R, Z_R orthogonal reference axis system with origin at theoretical confluence of parawing suspension lines and with Z_R-axis alined with theoretical 60-percent keel line (see fig. 1)

X_W, Y_W, Z_W axis system with origin at center of gravity of parawing and suspension lines and parallel to vehicle body axis system

y displacement along Y-axis, feet (meters)

α angle between X_B-axis and projection of relative wind vector in $X_B Z_B$-plane (referred to as angle of attack), radians or degrees

β angle between relative wind vector and $X_B Z_B$-plane (referred to as sideslip angle), radians or degrees

γ flight-path angle (that is, angle between inertial velocity vector and $X_C Y_C$-plane), radians or degrees

η_P, η_W, η_B displacement along Z_R-axis of center of gravity of payload, of parawing (including suspension lines), and of total composite body, respectively, feet (meters) (see fig. 1)

θ_O angle of optical axis of viewing system in $X_B Z_B$-plane measured from X_B-axis, degrees

λ direction of flight referenced to north, defined as angle between V_{XY}-axis and Y_C-axis, degrees

$\Delta\lambda$ heading error (that is, difference between heading into wind and actual flight-path direction), degrees

ξ_P, ξ_W, ξ_B displacement along X_R-axis of center of gravity of payload, of parawing (including suspension lines), and of total composite body, respectively, feet (meters) (see fig. 1)

ρ air density, slugs-foot^{-3} (kilograms-meter^{-3})

Φ angle between Y_B-axis and projection of relative wind vector in $Y_B Z_B$-plane (referred to as bank angle), radians or degrees

ψ, θ, ϕ Euler angles of rotation relating body axes and fixed-reference axis system, radians or degrees

$\Omega_X, \Omega_Y, \Omega_Z$ wind component along X-, Y-, and Z-axis, respectively, feet-second^{-1} (meters-second^{-1}) (see fig. 14)

Notation:

| | | absolute value

[ ]   square matrix

$\left\{ \ \right\}$ column matrix

$[\ ]^T$ transpose of matrix

$\left[\Gamma_{m-n}\right]_{\substack{m=B,C,I,O \\ n=B,C,I,O}}$ matrix which transforms a vector from axis system m to axis system n; B, C, I, and O represent body system, moving-reference system, fixed-reference system, and optics system, respectively

A dot over a symbol indicates a time derivative.

A prime denotes that the aerodynamic coefficient has been transferred to the center of gravity of the parawing-payload combination.

17

APPENDIX B

EQUATIONS OF MOTION

The simulation equipment used in the present study was a modification of the modification of the lunar orbit and landing approach simulator at the Langley Research Center. The form of the equations of motion was a result of the requirements of this equipment.

Force Equations

The equations of motion for the three translational degrees of freedom in the cylindrical coordinate system (fig. 14) are as follows:

$$\ddot{R} - R\dot{\Psi}^2 = -\frac{F_{ZC}}{m_B} - g_e\left(\frac{R_e}{R}\right)^2 \tag{B1}$$

$$R\ddot{\Psi} + 2\dot{R}\dot{\Psi} = \frac{F_{XC}}{m_B} \tag{B2}$$

$$\ddot{Y} = \frac{F_{YC}}{m_B} \tag{B3}$$

where F_{XC}, F_{YC}, and F_{ZC} are the aerodynamic forces along the X_C-, Y_C-, and Z_C-axes and are given by

$$\begin{Bmatrix} F_{XC} \\ F_{YC} \\ F_{ZC} \end{Bmatrix} = \begin{bmatrix} \Gamma_{C-B} \end{bmatrix}^T \begin{Bmatrix} F_{XB} \\ F_{YB} \\ F_{ZB} \end{Bmatrix} \tag{B4}$$

with

$$F_{XB} = QS\left(C'_{X,0} + C'_{X_\alpha}\alpha + C'_{X_q}\frac{qb}{2V_R} + \frac{\partial C'_X}{\partial \frac{\Delta l}{l_k}}\frac{\Delta l}{l_k} + \frac{\partial C'_X}{\partial \left|\frac{\Delta L}{l_k}\right|}\left|\frac{\Delta L}{l_k}\right|\right) \tag{B5}$$

$$F_{YB} = QS\left(C'_{Y_\beta}\beta + C'_{Y_p}\frac{pb}{2V_R} + C'_{Y_r}\frac{rb}{2V_R} + \frac{\partial C'_Y}{\partial\frac{\Delta L}{l_k}}\frac{\Delta L}{l_k} + \frac{\partial C'_{Y_\beta}}{\partial\left|\frac{\Delta L}{l_k}\right|}\beta\left|\frac{\Delta L}{l_k}\right|\right) \tag{B6}$$

and

$$F_{ZB} = QS\left(C'_{Z,0} + C'_{Z_\alpha}\alpha + C'_{Z_q}\frac{qb}{2V_R} + \frac{\partial C'_Z}{\partial\frac{\Delta l}{l_k}}\frac{\Delta l}{l_k} + \frac{\partial C'_Z}{\partial\left|\frac{\Delta L}{l_k}\right|}\left|\frac{\Delta L}{l_k}\right|\right) \tag{B7}$$

The matrix relating the moving-reference axis system to the body axis system is orthogonal and is

$$\left[\Gamma_{C-B}\right] = \left[\Gamma_{I-B}\right]\left[\Gamma_{C-I}\right] \tag{B8}$$

where

$$\left[\Gamma_{C-I}\right] = \begin{bmatrix} \cos\Psi & 0 & -\sin\Psi \\ 0 & 1 & 0 \\ \sin\Psi & 0 & \cos\Psi \end{bmatrix} \tag{B9}$$

and

$$\left[\Gamma_{I-B}\right] = \begin{bmatrix} A_{11} & A_{12} & A_{13} \\ A_{21} & A_{22} & A_{23} \\ A_{31} & A_{32} & A_{33} \end{bmatrix} \tag{B10}$$

The direction cosines are given in terms of quaternions by

$$A_{11} = 2\left(c^2 + f^2\right) - 1 \tag{B11}$$

$$A_{12} = 2(cd + ef) \tag{B12}$$

$$A_{13} = 2(ce - df) \tag{B13}$$

$$A_{21} = 2(cd - ef) \tag{B14}$$

$$A_{22} = 2\left(d^2 + f^2\right) - 1 \tag{B15}$$

$$A_{23} = 2(cf + de) \tag{B16}$$

$$A_{31} = 2(ce + df) \tag{B17}$$

$$A_{32} = 2(de - cf) \tag{B18}$$

$$A_{33} = 2\left(e^2 + f^2\right) - 1 \tag{B19}$$

and

$$\dot{c} = \frac{1}{2} (fp - eq + dr) + Kgc \tag{B20}$$

$$\dot{d} = \frac{1}{2} (ep + fq - cr) + Kgd \tag{B21}$$

$$\dot{e} = \frac{1}{2} (-dp + cq + fr) + Kge \tag{B22}$$

$$\dot{f} = -\frac{1}{2} (cp + dq + er) + Kgf \tag{B23}$$

where

$$g = 1 - \left(c^2 + d^2 + e^2 + f^2\right) \tag{B24}$$

and   K   is a gain factor determined empirically on the computer.

Moment Equations

The equations of motion for the three rotational degrees of freedom in the body-axis system are as follows:

$$\dot{p} = \frac{1}{I_{XB}}\left[M_{XB} + \left(I_{YB} - I_{ZB}\right)qr\right] \tag{B25}$$

$$\dot{q} = \frac{1}{I_{YB}}\left[M_{YB} + \left(I_{ZB} - I_{XB}\right)rp\right] \tag{B26}$$

$$\dot{r} = \frac{1}{I_{ZB}}\left[M_{ZB} + \left(I_{XB} - I_{YB}\right)pq\right] \tag{B27}$$

The aerodynamic moments are given by

$$M_{XB} = QSb\left(C'_{l_\beta}\beta + C'_{l_p}\frac{pb}{2V_R} + C'_{l_r}\frac{rb}{2V_R} + \frac{\partial C'_l}{\partial \frac{\Delta L}{l_k}}\frac{\Delta L}{l_k} + \frac{\partial C'_{l_\beta}}{\partial \left|\frac{\Delta L}{l_k}\right|}\beta\left|\frac{\Delta L}{l_k}\right|\right) \tag{B28}$$

$$M_{YB} = QSb\left(C'_{m,0} + C'_{m_\alpha}\alpha + C'_{m_q}\frac{qb}{2V_R} + \frac{\partial C'_m}{\partial \frac{\Delta l}{l_k}}\frac{\Delta l}{l_k} + \frac{\partial C'_m}{\partial \left|\frac{\Delta L}{l_k}\right|}\left|\frac{\Delta L}{l_k}\right|\right) \tag{B29}$$

and

$$M_{ZB} = QSb\left(C'_{n_\beta}\beta + C'_{n_p}\frac{pb}{2V_R} + C'_{n_r}\frac{rb}{2V_R} + \frac{\partial C'_n}{\partial \frac{\Delta L}{l_k}}\frac{\Delta L}{l_k} + \frac{\partial C'_{n_\beta}}{\partial \left|\frac{\Delta L}{l_k}\right|}\beta\left|\frac{\Delta L}{l_k}\right|\right) \tag{B30}$$

Auxiliary Equations

The matrix which transforms a vector from the moving-reference axis system to the optical axis system is

$$\left[\Gamma_{C-O}\right] = \begin{bmatrix} \gamma_{11} & \gamma_{12} & \gamma_{13} \\ \gamma_{21} & \gamma_{22} & \gamma_{23} \\ \gamma_{31} & \gamma_{32} & \gamma_{33} \end{bmatrix} = \left[\Gamma_{B-O}\right]\left[\Gamma_{C-B}\right] \tag{B31}$$

where

$$\left[\Gamma_{B-O}\right] = \begin{bmatrix} \cos\theta_O & 0 & \sin\theta_O \\ 0 & 1 & 0 \\ -\sin\theta_O & 0 & \cos\theta_O \end{bmatrix} \tag{B32}$$

21

and γ_{ij} are direction cosines relating the optical axis system to the moving-reference axis system. Thus, the angles $\overline{\psi}$, $\overline{\theta}$, and $\overline{\phi}$ used to drive the optical pickup are

$$\left.\begin{array}{l} \sin\overline{\theta} = -\gamma_{13} \\[2ex] \cos\overline{\theta} = + \sqrt{1 - \left(\gamma_{13}\right)^2} \end{array}\right\} \qquad \left(-\frac{\pi}{2} < \overline{\theta} < \frac{\pi}{2}\right) \qquad \text{(B33)}$$

$$\left.\begin{array}{l} \sin\overline{\phi} = \dfrac{\gamma_{23}}{\cos\overline{\theta}} \\[3ex] \cos\overline{\phi} = \dfrac{\gamma_{33}}{\cos\overline{\theta}} \end{array}\right\} \qquad \text{(B34)}$$

$$\left.\begin{array}{l} \sin\overline{\psi} = \dfrac{\gamma_{12}}{\cos\overline{\theta}} \\[3ex] \cos\overline{\psi} = \dfrac{\gamma_{11}}{\cos\overline{\theta}} \end{array}\right\} \qquad \text{(B35)}$$

Dynamic pressure is given by

$$Q = \frac{1}{2}\rho V_R^2 \qquad \text{(B36)}$$

where

$$V_R = \sqrt{\left(u + \Omega_{XB}\right)^2 + \left(v + \Omega_{YB}\right)^2 + \left(w + \Omega_{ZB}\right)^2} \qquad \text{(B37)}$$

and

$$\left\{\begin{array}{c} \Omega_{XB} \\ \Omega_{YB} \\ \Omega_{ZB} \end{array}\right\} = \left[\Gamma_{I-B}\right] \left\{\begin{array}{c} \Omega_X \\ \Omega_Y \\ \Omega_Z \end{array}\right\} \qquad \text{(B38)}$$

$$
\begin{Bmatrix} u \\ v \\ w \end{Bmatrix} = \begin{bmatrix} \Gamma_{C\text{-}B} \end{bmatrix} \begin{Bmatrix} \dot{X}_C \\ \dot{Y}_C \\ \dot{Z}_C \end{Bmatrix}
\tag{B39}
$$

with

$$
\left.\begin{aligned}
\dot{X}_C &= R\dot{\Psi} \\[2ex]
\dot{Y}_C &= \dot{Y} \\[2ex]
\dot{Z}_C &= -\dot{R}
\end{aligned}\right\}
\tag{B40}
$$

Angle of attack, sideslip angle, flight-path angle, bank angle, and altitude are expressed as follows:

$$
\left.\begin{aligned}
\sin \alpha &= \frac{w + \Omega_{ZB}}{\sqrt{\left(u + \Omega_{XB}\right)^2 + \left(w + \Omega_{ZB}\right)^2}} \\[3ex]
\cos \alpha &= \frac{u + \Omega_{XB}}{\sqrt{\left(u + \Omega_{XB}\right)^2 + \left(w + \Omega_{ZB}\right)^2}}
\end{aligned}\right\}
\tag{B41}
$$

$$
\left.\begin{aligned}
\sin \beta &= \frac{v + \Omega_{YB}}{V_R} \\[3ex]
\cos \beta &= \frac{\sqrt{\left(u + \Omega_{XB}\right)^2 + \left(w + \Omega_{XB}\right)^2}}{V_R}
\end{aligned}\right\}
\tag{B42}
$$

$$\left.\begin{array}{l} \sin \gamma = \dfrac{\dot{Z}_C}{\sqrt{\left(\dot{X}_C\right)^2 + \left(\dot{Y}_C\right)^2 + \left(\dot{Z}_C\right)^2}} \\[3em] \cos \gamma = \dfrac{\sqrt{\left(\dot{X}_C\right)^2 + \left(\dot{Y}_C\right)^2}}{\sqrt{\left(\dot{X}_C\right)^2 + \left(\dot{Y}_C\right)^2 + \left(\dot{Z}_C\right)^2}} \end{array}\right\} \tag{B43}$$

$$\left.\begin{array}{l} \sin \Phi = \dfrac{w + \Omega_{ZB}}{\sqrt{\left(v + \Omega_{YB}\right)^2 + \left(w + \Omega_{ZB}\right)^2}} \\[3em] \cos \Phi = \dfrac{v + \Omega_{YB}}{\sqrt{\left(v + \Omega_{YB}\right)^2 + \left(w + \Omega_{ZB}\right)^2}} \end{array}\right\} \tag{B44}$$

$$\left.\begin{array}{l} h = R - 20.9 \times 10^6 \text{ ft} \\[1.5em] h = R - 6.37 \times 10^6 \text{ m} \end{array}\right\} \tag{B45}$$

TRANSFER EQUATIONS

The computer program used in the present investigation included the following equations to transfer the basic aerodynamic derivatives, which were referenced to the theoretical confluence of the suspension lines (fig. 1), to the center of gravity of the parawing-payload combination:

$$C'_{Y_\beta} = C_{Y_\beta} \tag{C1}$$

$$C'_{Y_p} = C_{Y_p} - 2C_{Y_\beta} \frac{\eta_B}{b} \tag{C2}$$

$$C'_{Y_r} = C_{Y_r} + 2C_{Y_\beta} \frac{\xi_B}{b} \tag{C3}$$

$$C'_{l_\beta} = C_{l_\beta} - C_{Y_\beta} \frac{\eta_B}{b} \tag{C4}$$

$$C'_{l_p} = C_{l_p} - 2C_{l_\beta} \frac{\eta_B}{b} - C_{Y_p} \frac{\eta_B}{b} + 2C_{Y_\beta} \left(\frac{\eta_B}{b}\right)^2 \tag{C5}$$

$$C'_{l_r} = C_{l_r} + 2C_{l_\beta} \frac{\xi_B}{b} - C_{Y_r} \frac{\eta_B}{b} - 2C_{Y_\beta} \frac{\xi_B \eta_B}{b^2} \tag{C6}$$

$$C'_{n_\beta} = C_{n_\beta} + C_{Y_\beta} \frac{\xi_B}{b} \tag{C7}$$

$$C'_{n_p} = C_{n_p} - 2C_{n_\beta} \frac{\eta_B}{b} + C_{Y_p} \frac{\xi_B}{b} - 2C_{Y_\beta} \frac{\xi_B \eta_B}{b^2} \tag{C8}$$

$$C'_{n_r} = C_{n_r} + 2C_{n_\beta} \frac{\xi_B}{b} + C_{Y_r} \frac{\xi_B}{b} + 2C_{Y_\beta} \left(\frac{\xi_B}{b}\right)^2 \tag{C9}$$

$$C'_{X,0} + C'_{X_\alpha}\alpha = C_{X,0} + C_{X_\alpha}\alpha \tag{C10}$$

$$C'_{X_q} = C_{X_q} - 2C_{X_\alpha} \frac{\xi_B}{b} \tag{C11}$$

$$C'_{Z,0} + C'_{Z_\alpha} \alpha = C_{Z,0} + C_{Z_\alpha} \alpha \tag{C12}$$

$$C'_{Z_q} = C_{Z_q} - 2C_{Z_\alpha} \frac{\xi_B}{b} \tag{C13}$$

$$C'_{m,0} + C'_{m_\alpha} \alpha = C_{m,0} + C_{m_\alpha} \alpha + \left(C_{X,0} + C_{X_\alpha} \alpha \right) \frac{\eta_B}{b} - \left(C_{Z,0} + C_{Z_\alpha} \alpha \right) \frac{\xi_B}{b} \tag{C14}$$

$$C'_{m_q} = C_{m_q} - 2C_{m_\alpha} \frac{\xi_B}{b} + C_{X_q} \frac{\eta_B}{b} - 2C_{X_\alpha} \frac{\xi_B \eta_B}{b^2} - C_{Z_q} \frac{\xi_B}{b} + 2C_{Z_\alpha} \left(\frac{\xi_B}{b} \right)^2 \tag{C15}$$

$$\frac{\partial C'_X}{\partial \left| \frac{\Delta L}{l_k} \right|} = \frac{\partial C_X}{\partial \left| \frac{\Delta L}{l_k} \right|} \tag{C16}$$

$$\frac{\partial C'_Z}{\partial \left| \frac{\Delta L}{l_k} \right|} = \frac{\partial C_Z}{\partial \left| \frac{\Delta L}{l_k} \right|} \tag{C17}$$

$$\frac{\partial C'_m}{\partial \left| \frac{\Delta L}{l_k} \right|} = \frac{\partial C_m}{\partial \left| \frac{\Delta L}{l_k} \right|} + \frac{\partial C_X}{\partial \left| \frac{\Delta L}{l_k} \right|} \frac{\eta_B}{b} - \frac{\partial C_Z}{\partial \left| \frac{\Delta L}{l_k} \right|} \frac{\xi_B}{b} \tag{C18}$$

$$\frac{\partial C'_X}{\partial \frac{\Delta l}{l_k}} = \frac{\partial C_X}{\partial \frac{\Delta l}{l_k}} \tag{C19}$$

$$\frac{\partial C'_Z}{\partial \frac{\Delta l}{l_k}} = \frac{\partial C_Z}{\partial \frac{\Delta l}{l_k}} \tag{C20}$$

$$\frac{\partial C'_m}{\partial \frac{\Delta l}{l_k}} = \frac{\partial C_m}{\partial \frac{\Delta l}{l_k}} + \frac{\partial C_X}{\partial \frac{\Delta l}{l_k}} \frac{\eta_B}{b} - \frac{\partial C_Z}{\partial \frac{\Delta l}{l_k}} \frac{\xi_B}{b} \tag{C21}$$

26

$$\frac{\partial C_Y'}{\partial \dfrac{\Delta L}{l_k}} = \frac{\partial C_Y}{\partial \dfrac{\Delta L}{l_k}} \tag{C22}$$

$$\frac{\partial C_n'}{\partial \dfrac{\Delta L}{l_k}} = \frac{\partial C_n}{\partial \dfrac{\Delta L}{l_k}} + \frac{\partial C_Y}{\partial \dfrac{\Delta L}{l_k}} \frac{\xi_B}{b} \tag{C23}$$

$$\frac{\partial C_l'}{\partial \dfrac{\Delta L}{l_k}} = \frac{\partial C_l}{\partial \dfrac{\Delta L}{l_k}} - \frac{\partial C_Y}{\partial \dfrac{\Delta L}{l_k}} \frac{\eta_B}{b} \tag{C24}$$

$$\frac{\partial C_{Y_\beta}'}{\partial \left|\dfrac{\Delta L}{l_k}\right|} = \frac{\partial C_{Y_\beta}}{\partial \left|\dfrac{\Delta L}{l_k}\right|} \tag{C25}$$

$$\frac{\partial C_{n_\beta}'}{\partial \left|\dfrac{\Delta L}{l_k}\right|} = \frac{\partial C_{n_\beta}}{\partial \left|\dfrac{\Delta L}{l_k}\right|} + \frac{\partial C_{Y_\beta}}{\partial \left|\dfrac{\Delta L}{l_k}\right|} \frac{\xi_B}{b} \tag{C26}$$

$$\frac{\partial C_{l_\beta}'}{\partial \left|\dfrac{\Delta L}{l_k}\right|} = \frac{\partial C_{l_\beta}}{\partial \left|\dfrac{\Delta L}{l_k}\right|} - \frac{\partial C_{Y_\beta}}{\partial \left|\dfrac{\Delta L}{l_k}\right|} \frac{\eta_B}{b} \tag{C27}$$

where

$$\xi_B = \left(\frac{m_W}{m_W + m_P}\right)\xi_W + \left(\frac{m_P}{m_W + m_P}\right)\xi_P \tag{C28}$$

$$\eta_B = \left(\frac{m_W}{m_W + m_P}\right)\eta_W + \left(\frac{m_P}{m_W + m_P}\right)\eta_P \tag{C29}$$

In addition, the moments of inertia of the parawing-payload combination about the X_B-, Y_B-, and Z_B-axes are given by

$$I_{XB} = I_{XP} + m_P\left(\eta_B - \eta_P\right)^2 + I_{XW} + \left(m_W + m_a\right)\left(\eta_W - \eta_B\right)^2 \tag{C30}$$

$$I_{YB} = I_{YP} + m_P \left[\left(\eta_B - \eta_P \right)^2 + \left(\xi_B - \xi_P \right)^2 \right]$$

$$+ I_{YW} + \left(m_W + m_a \right) \left[\left(\eta_W - \eta_B \right)^2 + \left(\xi_B - \xi_W \right)^2 \right] \tag{C31}$$

$$I_{ZB} = I_{ZP} + m_P \left(\xi_B - \xi_P \right)^2 + I_{ZW} + \left(m_a + m_P \right) \left(\xi_B - \xi_W \right)^2 \tag{C32}$$

REFERENCES

1. Miller, G. Kimball, Jr.; Jaquet, Byron M.; and Price, Douglas B.: Fixed-Base Visual Simulation of Pilot-Controlled Descents of an Advanced Apollo Spacecraft With an All-Flexible Parawing. NASA TN D-5049, 1969.

2. Mechtly, E. A.: The International System of Units — Physical Constants and Conversion Factors. NASA SP-7012, 1964.

3. Libbey, Charles E.; Ware, George M.; and Naeseth, Rodger L.: Wind-Tunnel Investigation of the Static Aerodynamic Characteristics of an 18-Foot (5.49-Meter) All-Flexible Parawing. NASA TN D-3856, 1967.

4. Sumners, Dan O.: Inertia Tests of a 24 Foot Single Keel Parawing — Model 1. NASA CR-66744, 1968.

5. Kaestner, P. T.: An Articulated Optical Pickup for Scale Model Simulation. J. SMPTE, vol. 76, no. 10, Oct. 1967, pp. 988-991.

6. Chambers, Joseph R.; and Boisseau, Peter C.: A Theoretical Analysis of the Dynamic Lateral Stability and Control of a Parawing Vehicle. NASA TN D-3461, 1966.

7. Robinson, Alfred C.: On the Use of Quaternions in Simulation of Rigid-Body Motion. WADC Tech. Rep. 58-17, U.S. Air Force, Dec. 1958. (Available from DDC as AD No. 234422.)
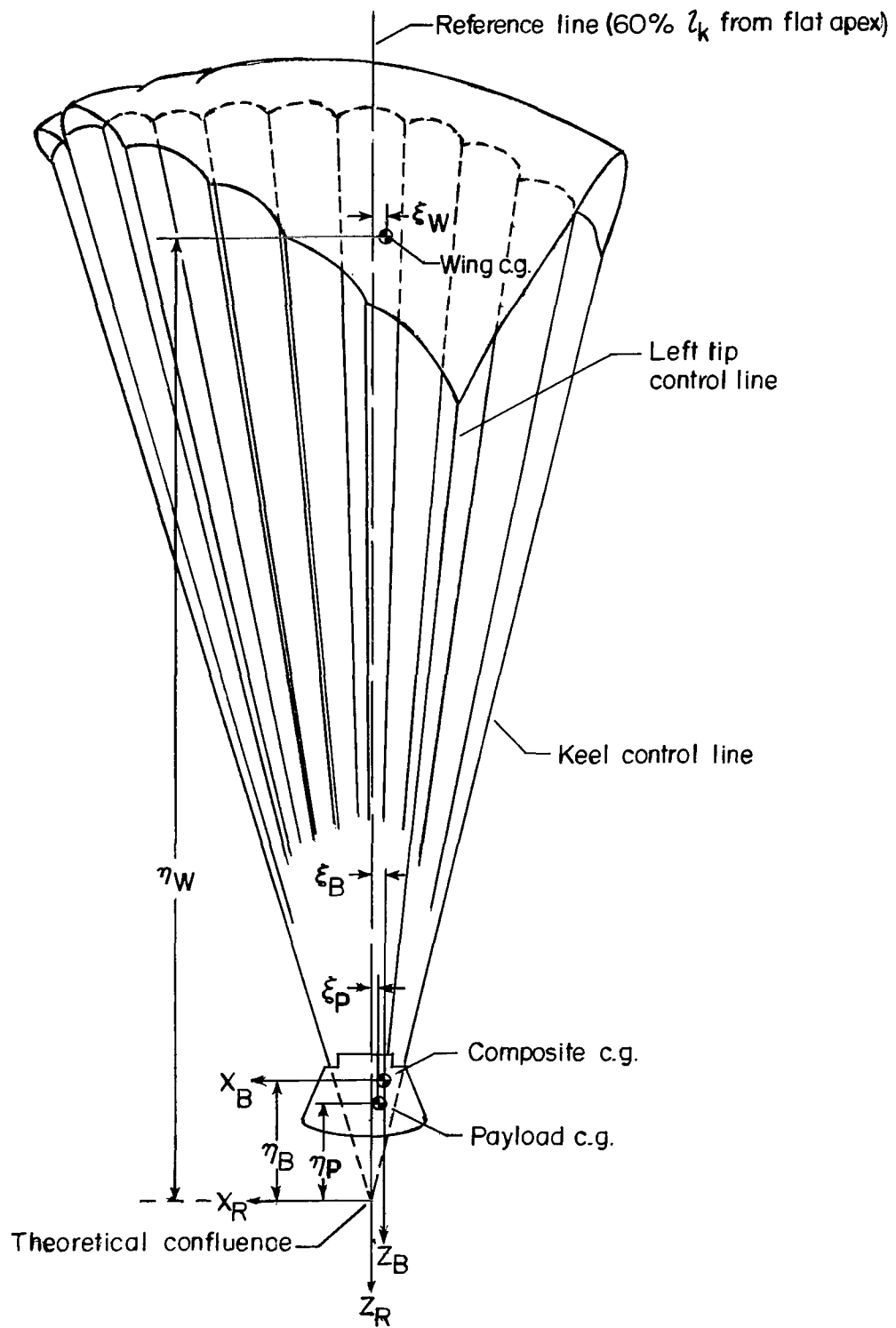
Figure 1.- Simulated vehicle configuration (not to scale).
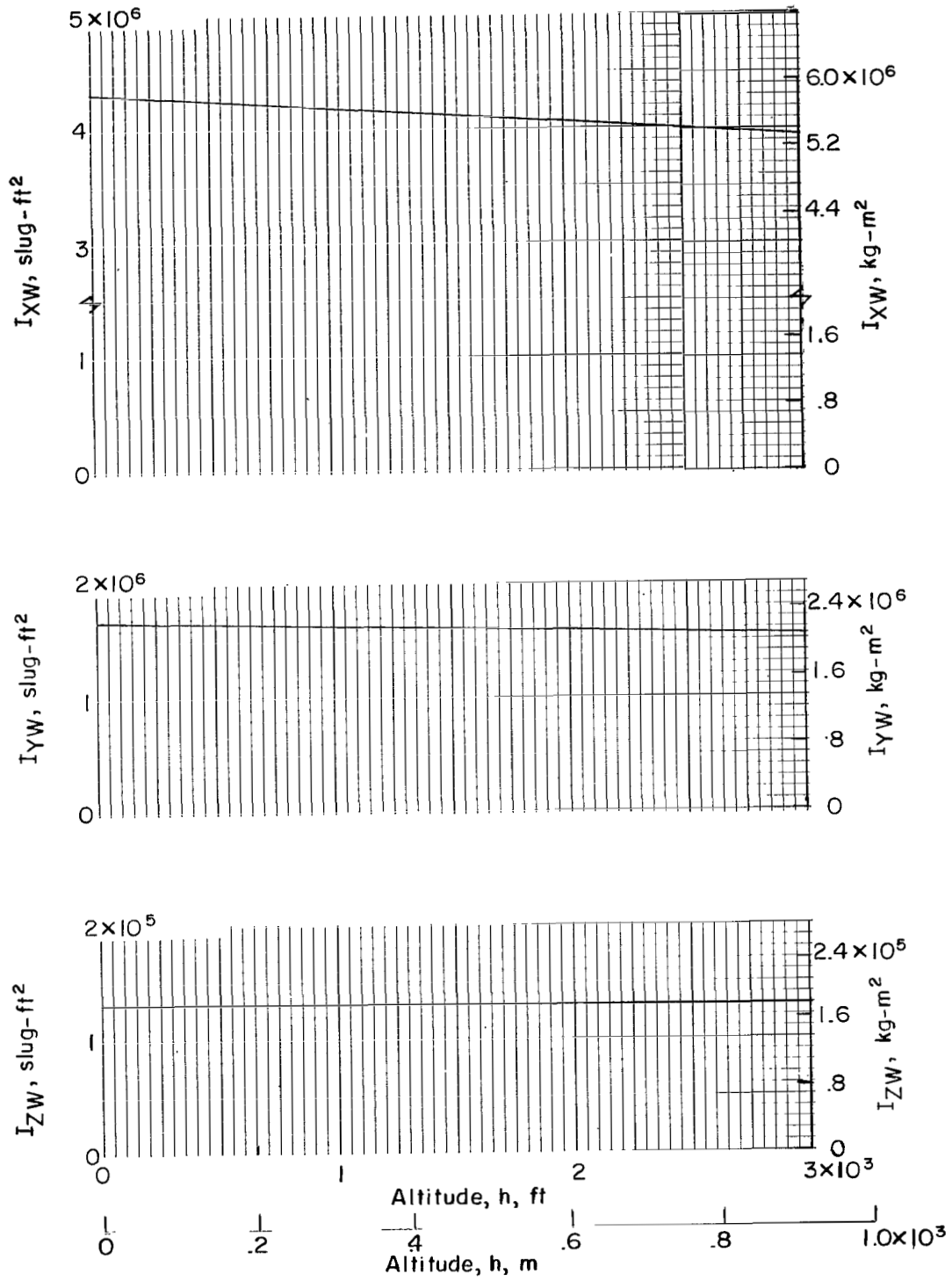
Figure 2.- Parawing moments of inertia (including wing fabric, suspension lines, and apparent inertia effects).

1. Optical viewing head

2. Image orthicon camera

3. Camera transport system
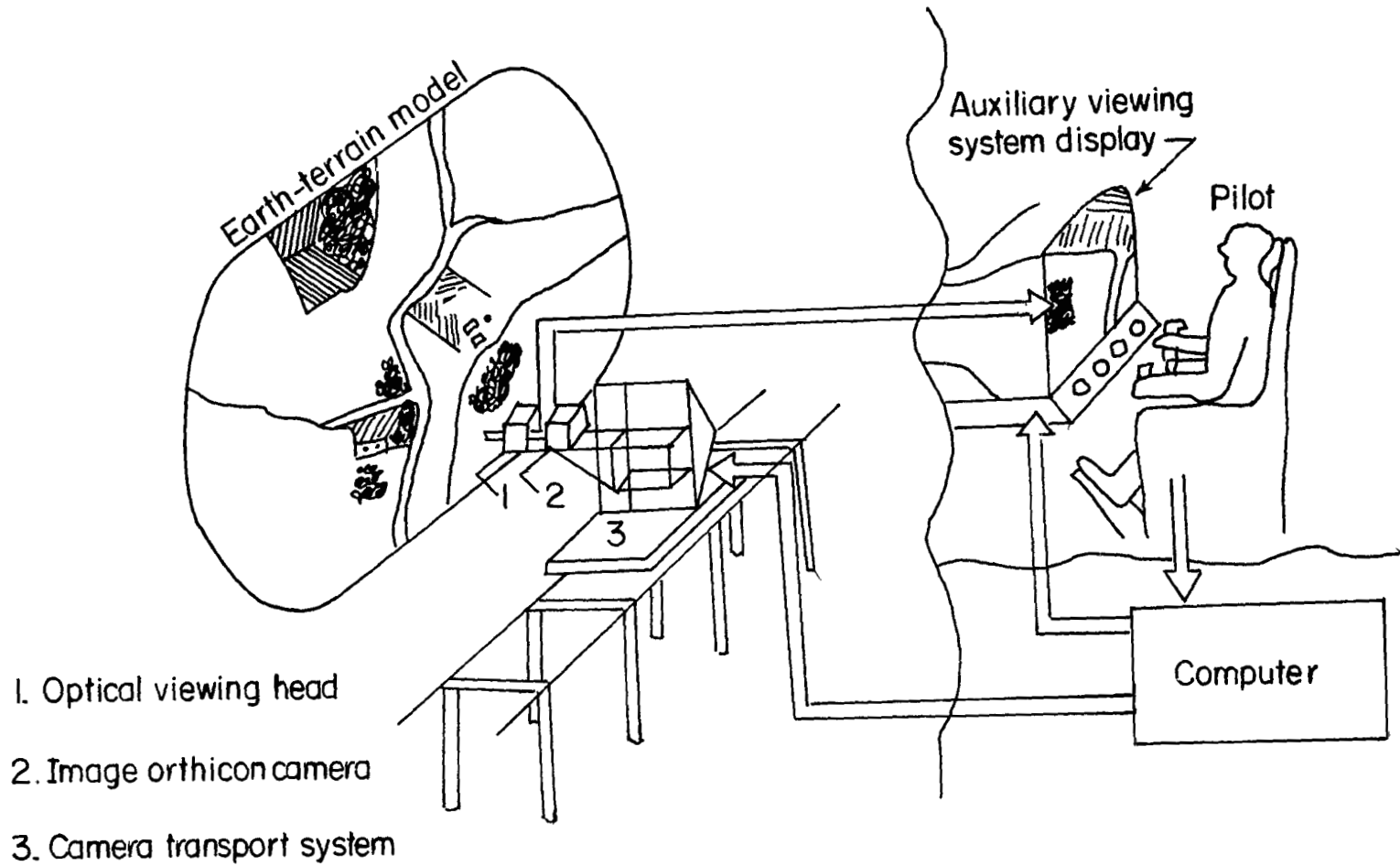
Figure 3.- Simulation equipment.

1. Attitude and angular rates
2. Angle of attack
3. Angle of sideslip
4. Flight path
5. Inertial velocity
6. Rate of descent
7. Altitude
8. Lateral trim inputs
9. Window angle and selector
10. Longitudinal trim inputs
11. Lateral control inputs
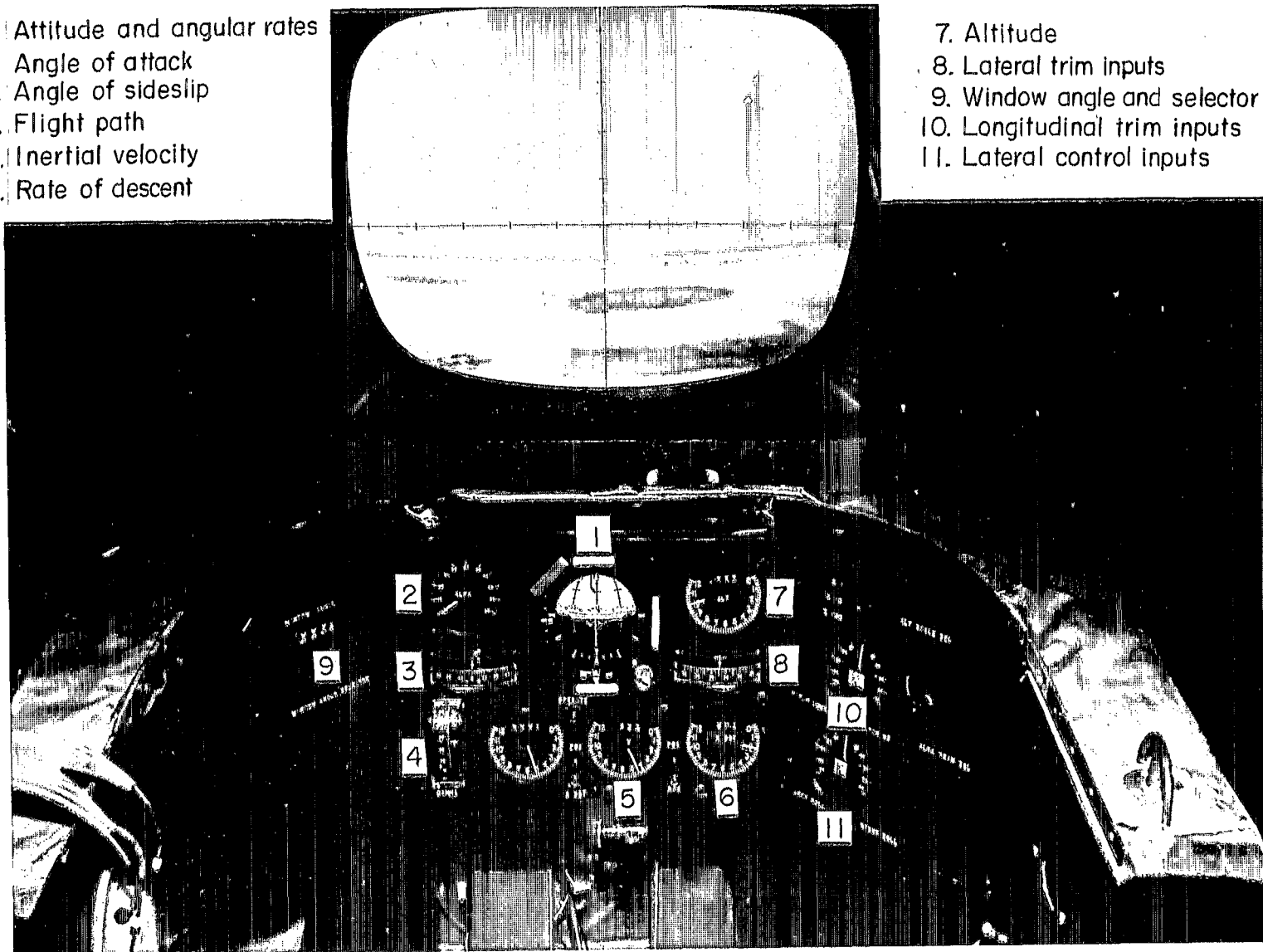
Figure 4.- Cockpit and instrumentation.

L-67-4666.1

Camera transport
system

Model

Figure 5.- Earth-terrain model and camera transport system.

L-69-7034.1
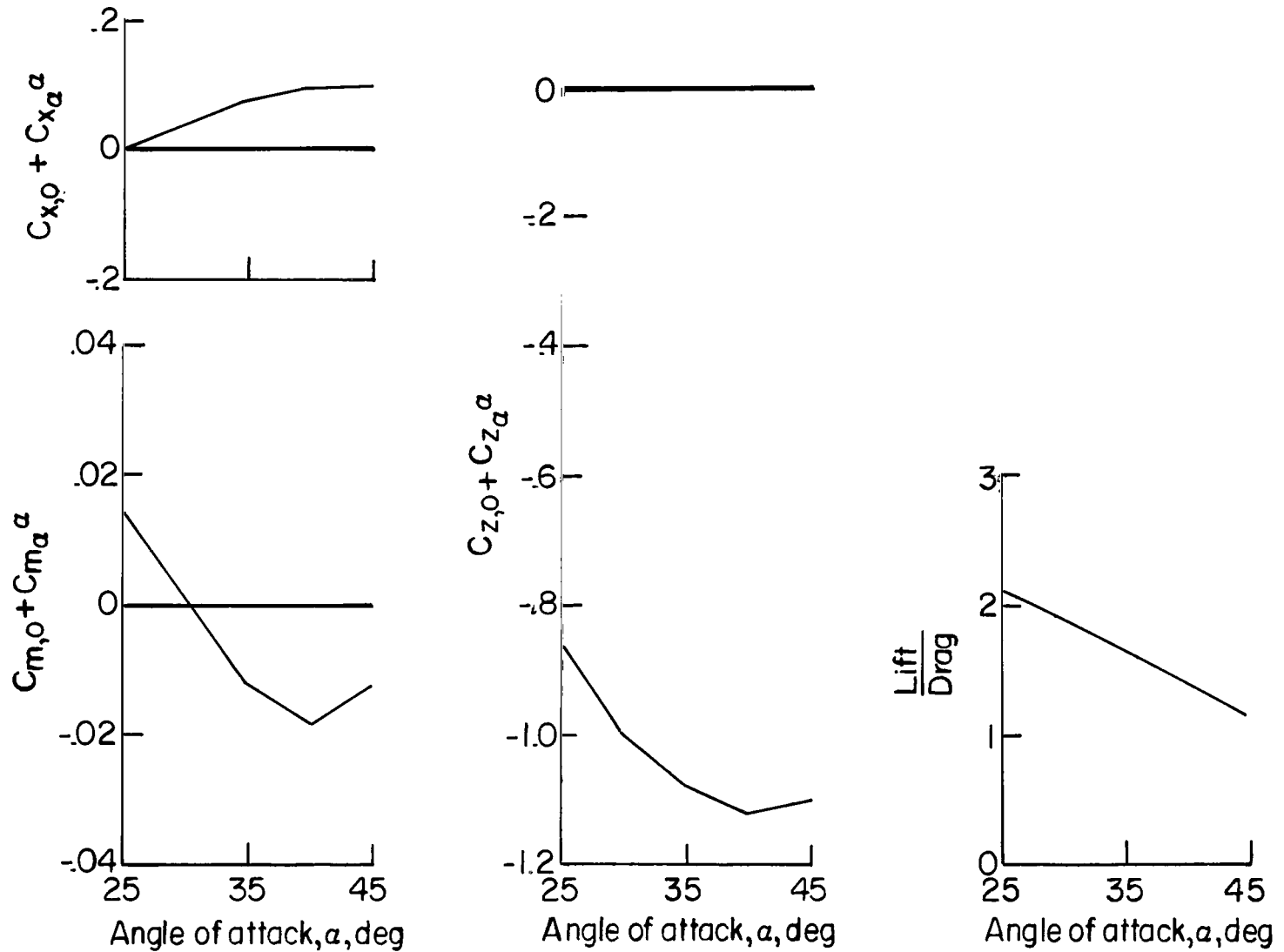
(a) Variation of longitudinal aerodynamic parameters and lift-drag ratio with α.

Figure 6.- Aerodynamic and control parameters used in simulation. Data are referenced to axis system located at the theoretical confluence of the suspension lines as shown in figure 1. All parameters are based on area and span of parawing when flat.
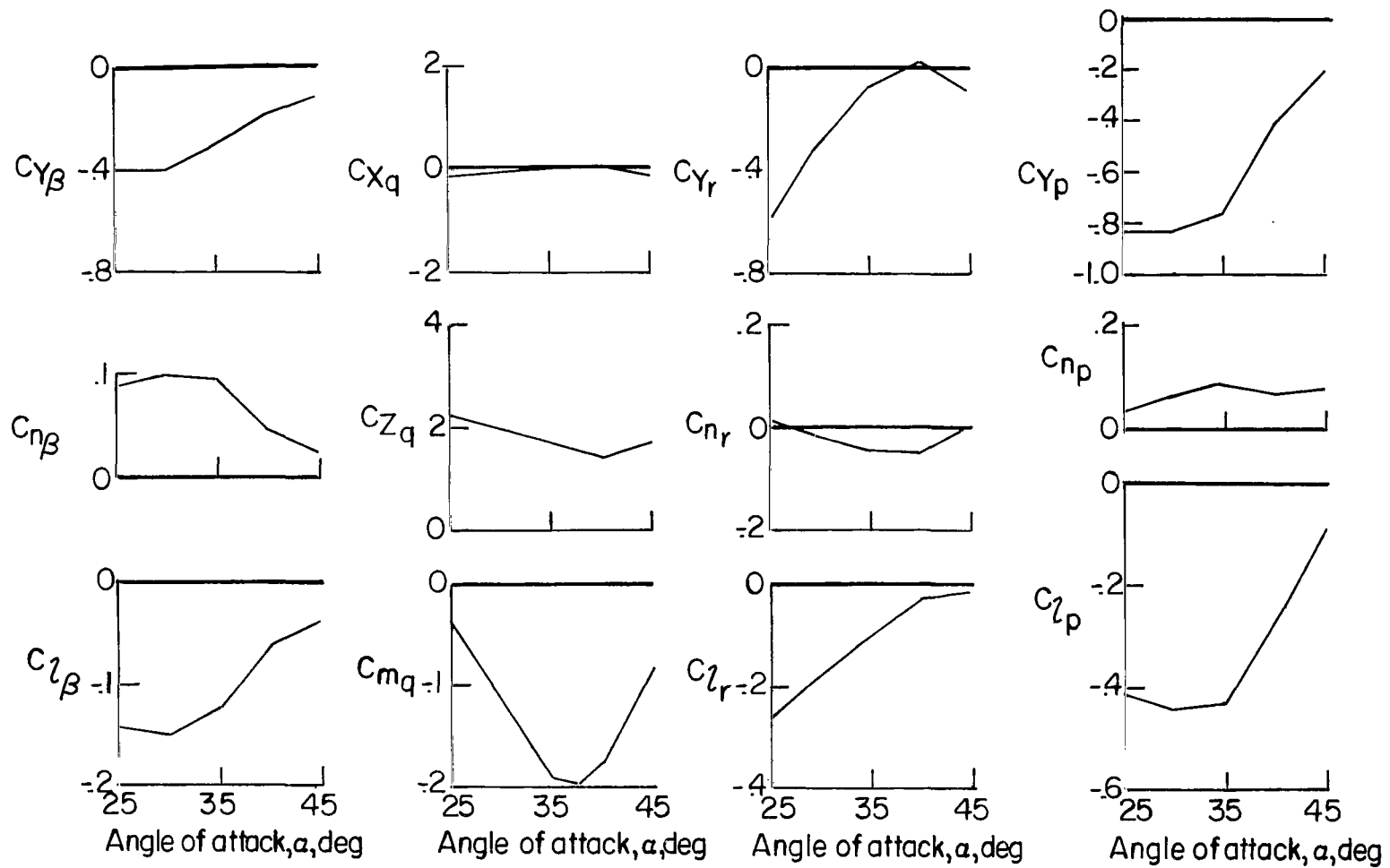
(b) Variation of β, q, r, and p derivatives with α for undeflected controls. (These parameters are combination derivatives obtained from measurements made during forced oscillation tests of a 5-ft (1.52-m) keel model.)

Figure 6.- Continued.
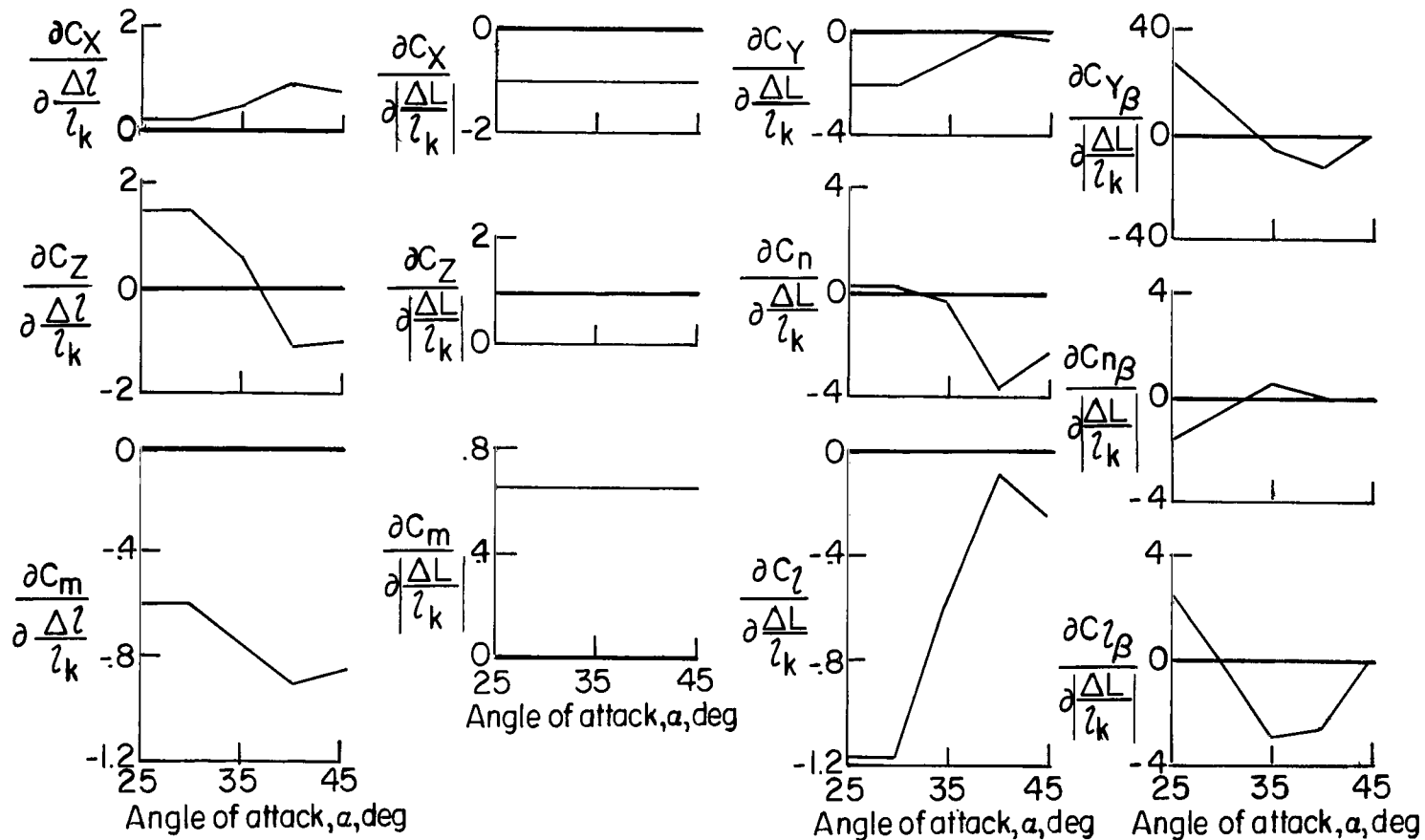
(c) Variation of control parameters with α.

Figure 6.- Concluded.
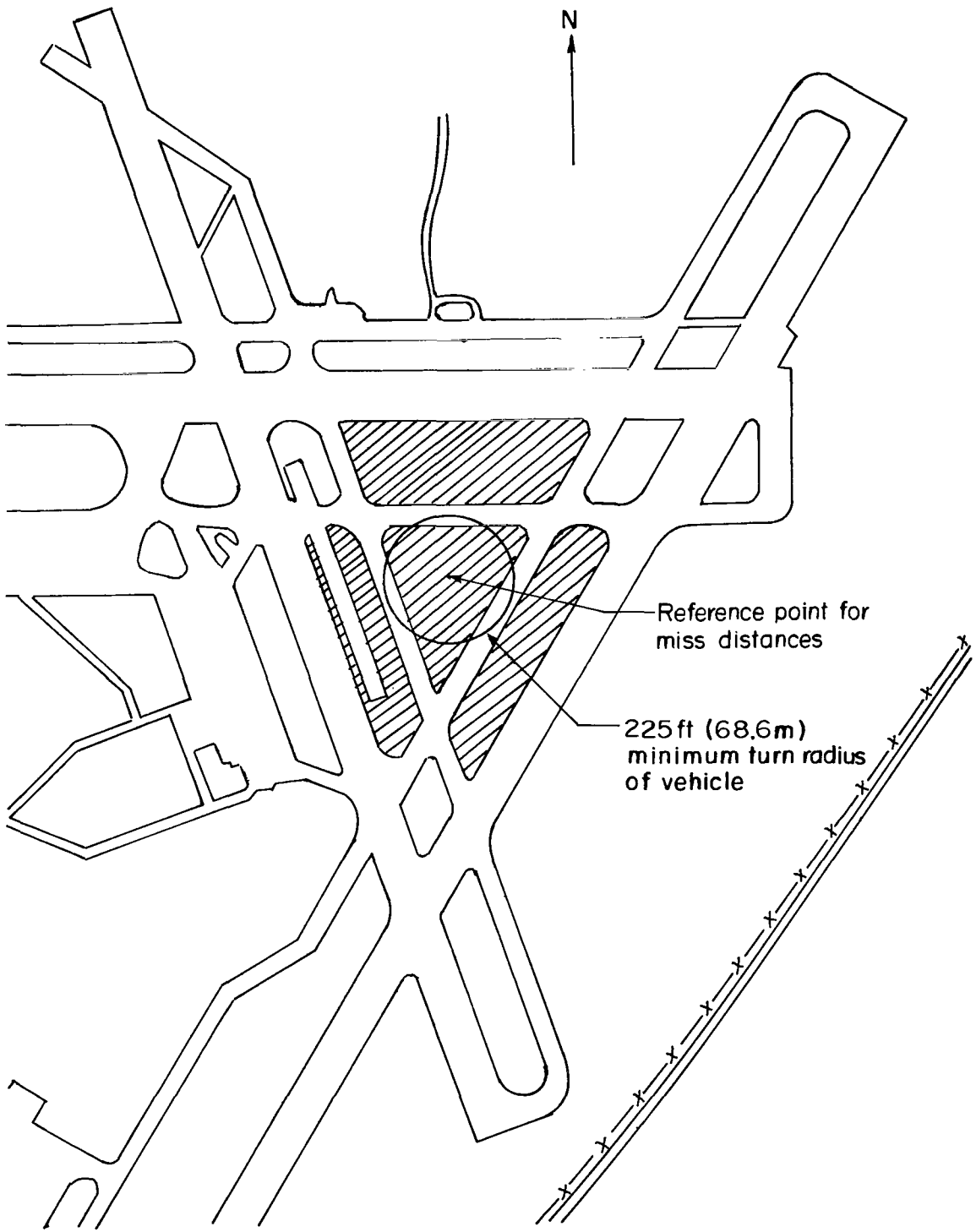
Figure 7.- Landing area. (Shading indicates acceptable landing sites.)
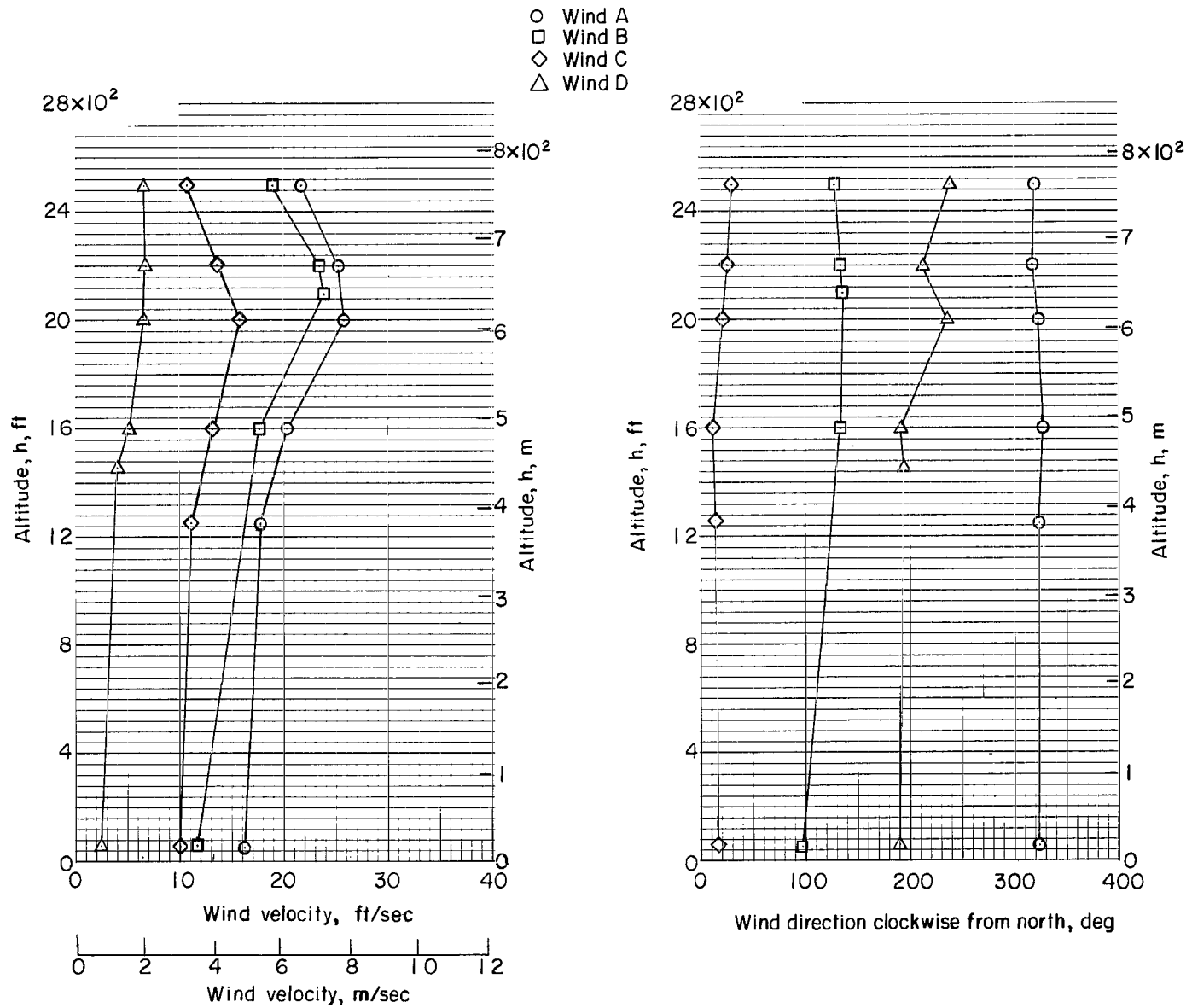
Figure 8.- Wind profiles.
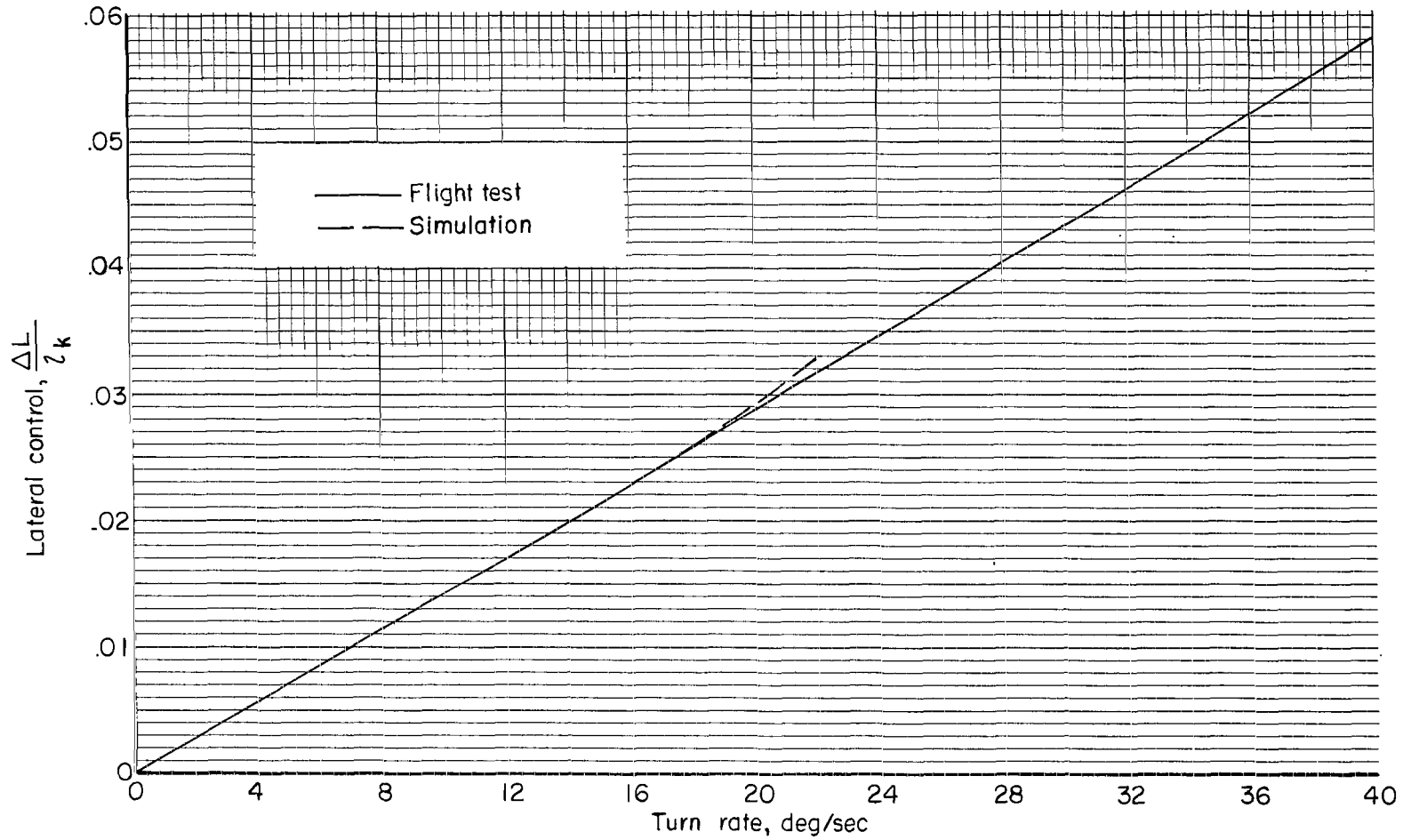
(a) Turn-rate capability.

Figure 9.- Flight-test and simulation results of a small-scale parawing.
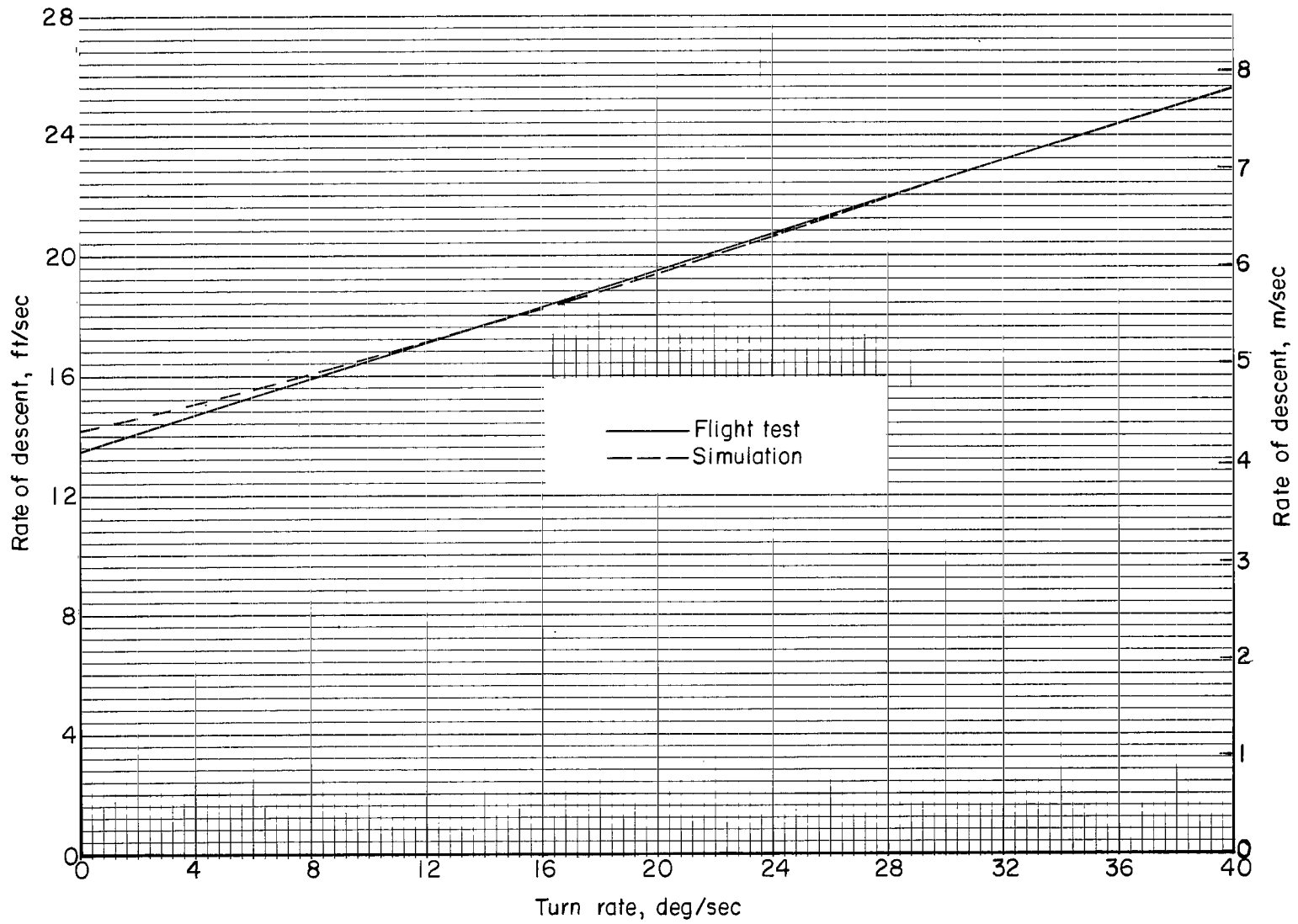
(b) Rate of descent as a function of turn rate.

Figure 9.- Concluded.
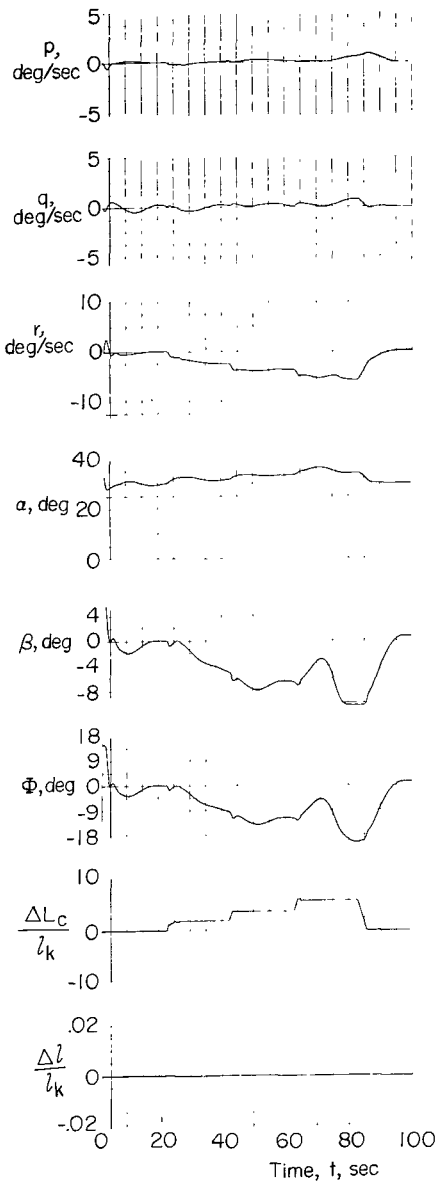
(a) Wing with zero apparent mass and moments of inertia as shown in figure 2.
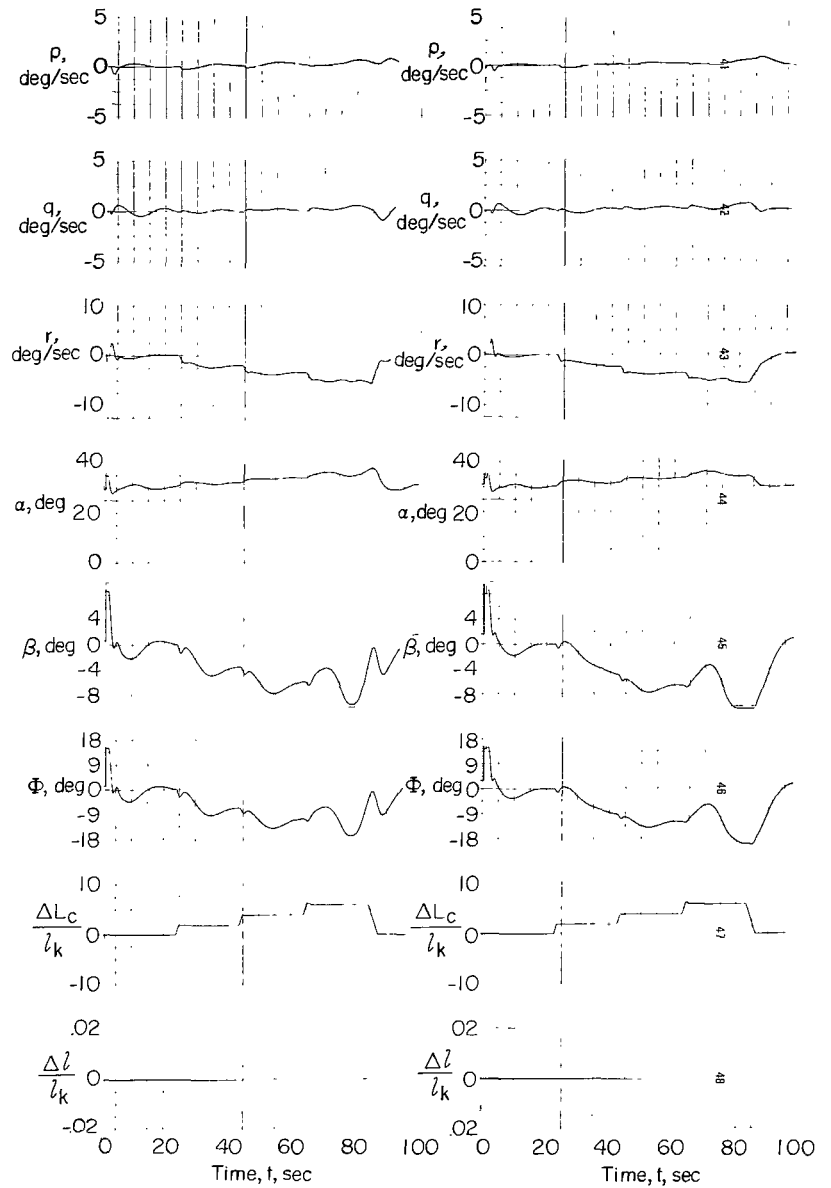
(b) Wing with apparent mass of 250 slugs (3648.5 kg) and moments of inertia as shown in figure 2.

(c) Wind with zero apparent mass and reduced moments of inertia.

Figure 10.- Apparent mass and inertia effects on vehicle flight characteristics.
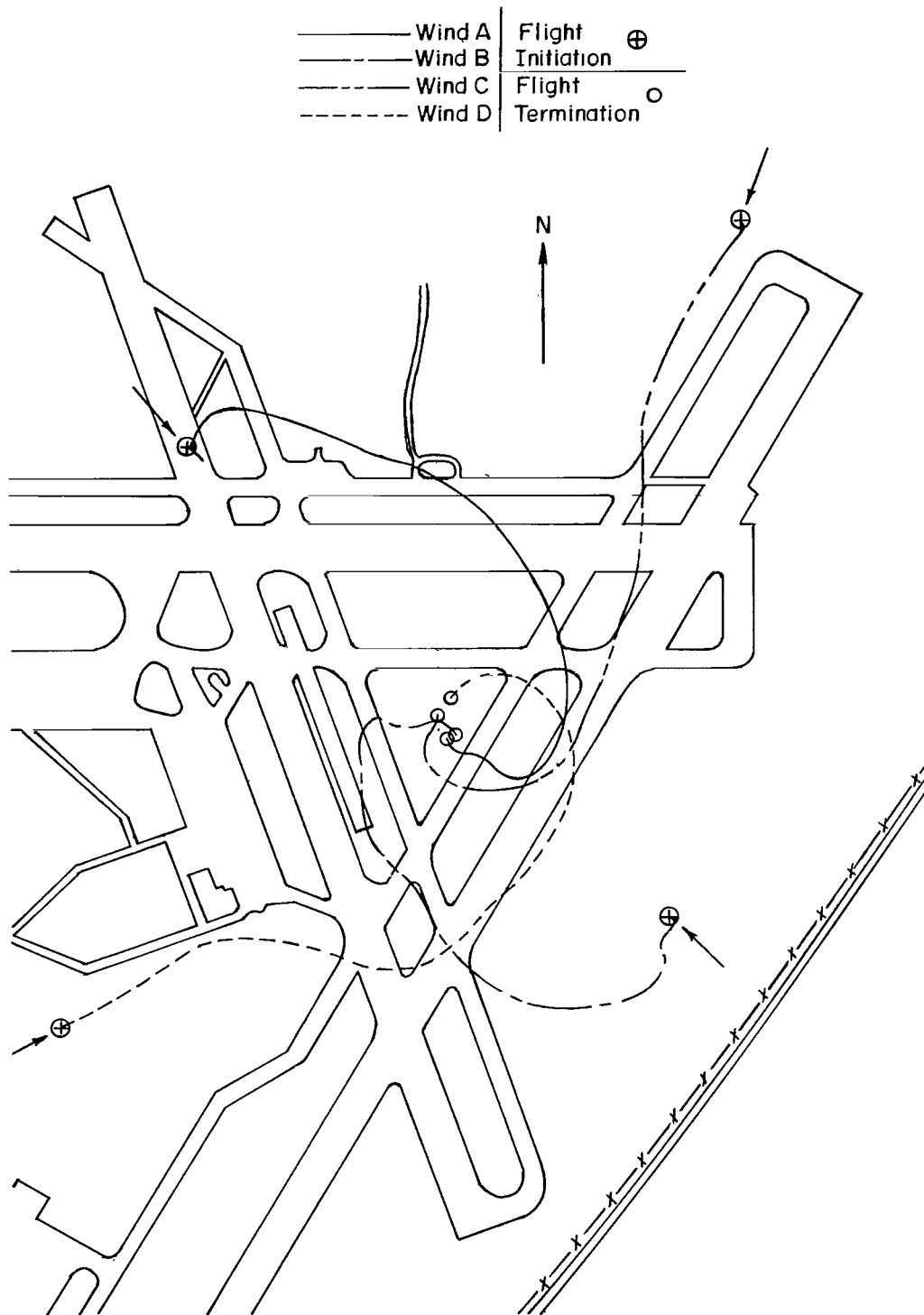
Figure 11.- Ground tracks of representative flights made under the influence of the four wind profiles used in the study. (Arrows denote wind direction at flight initiation.)
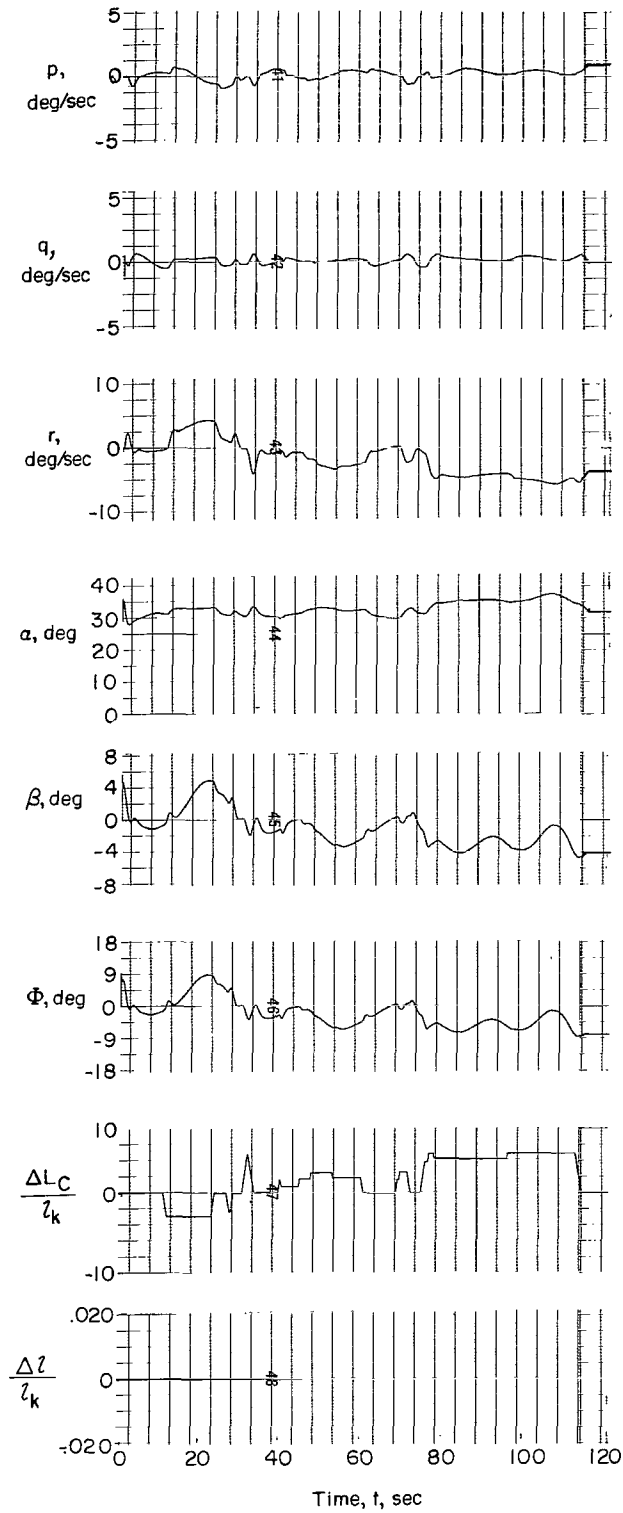
Figure 12.- Time history of representative flight made under the influence of low wind D. (Vertical displacements of ψ and λ denote scale changes of 180^0.)

44
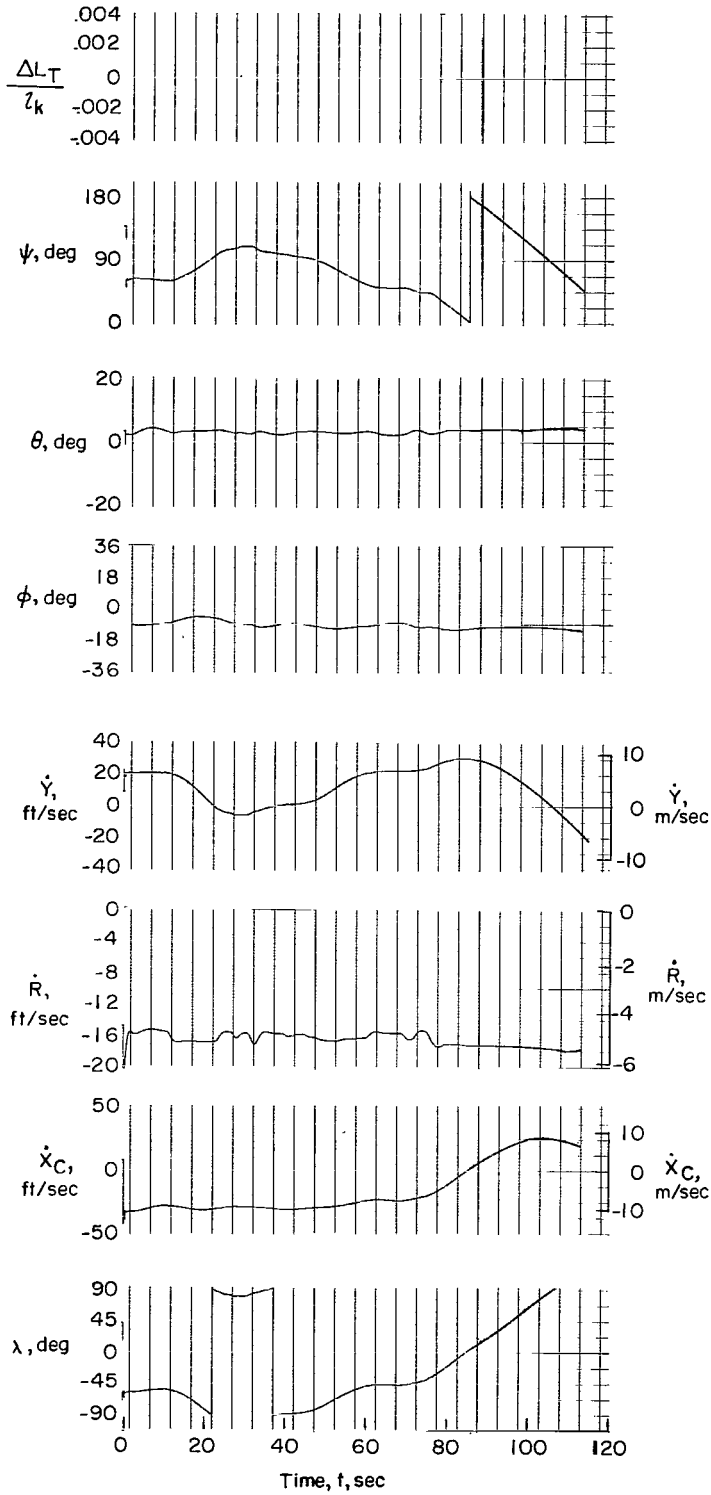
Figure 12.- Concluded.
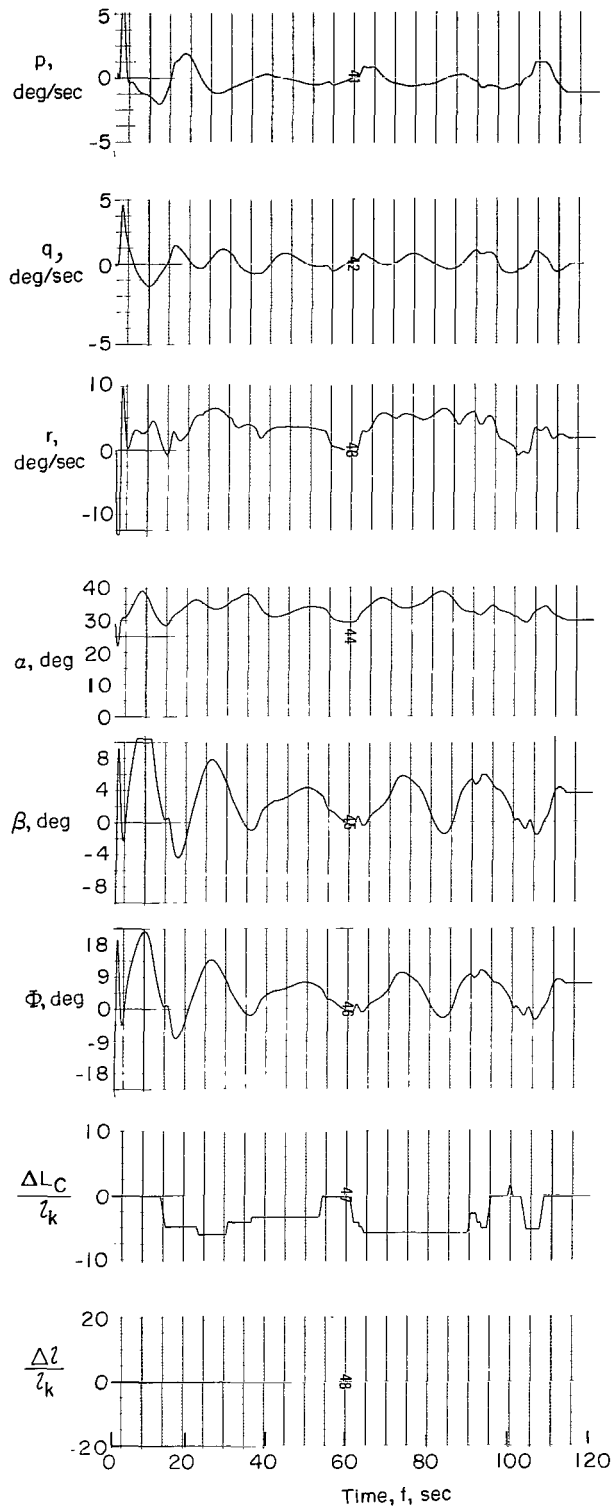
Figure 13.- Time history of representative flight made under the influence of high wind A. (Vertical displacements of ψ and λ denote scale changes of 180^{0}.)
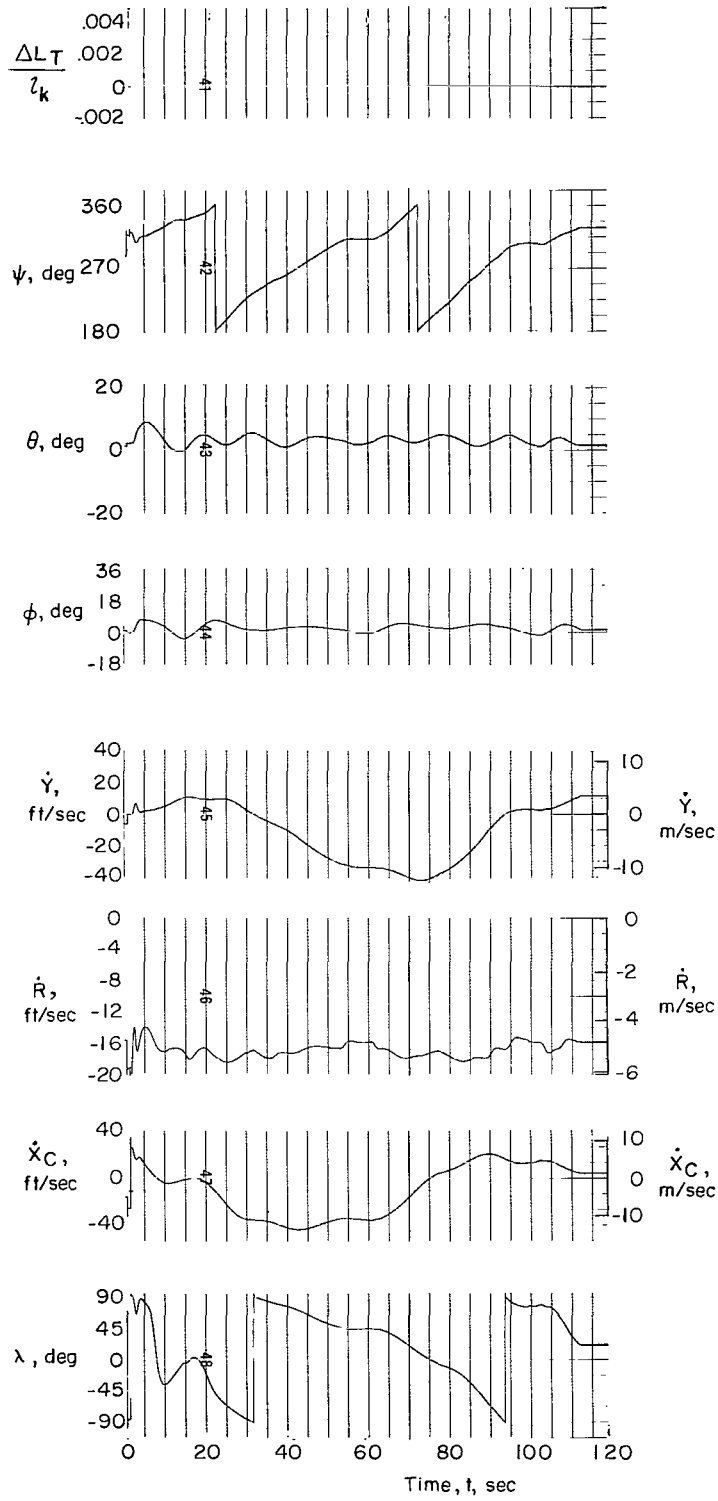
Figure 13.- Concluded.
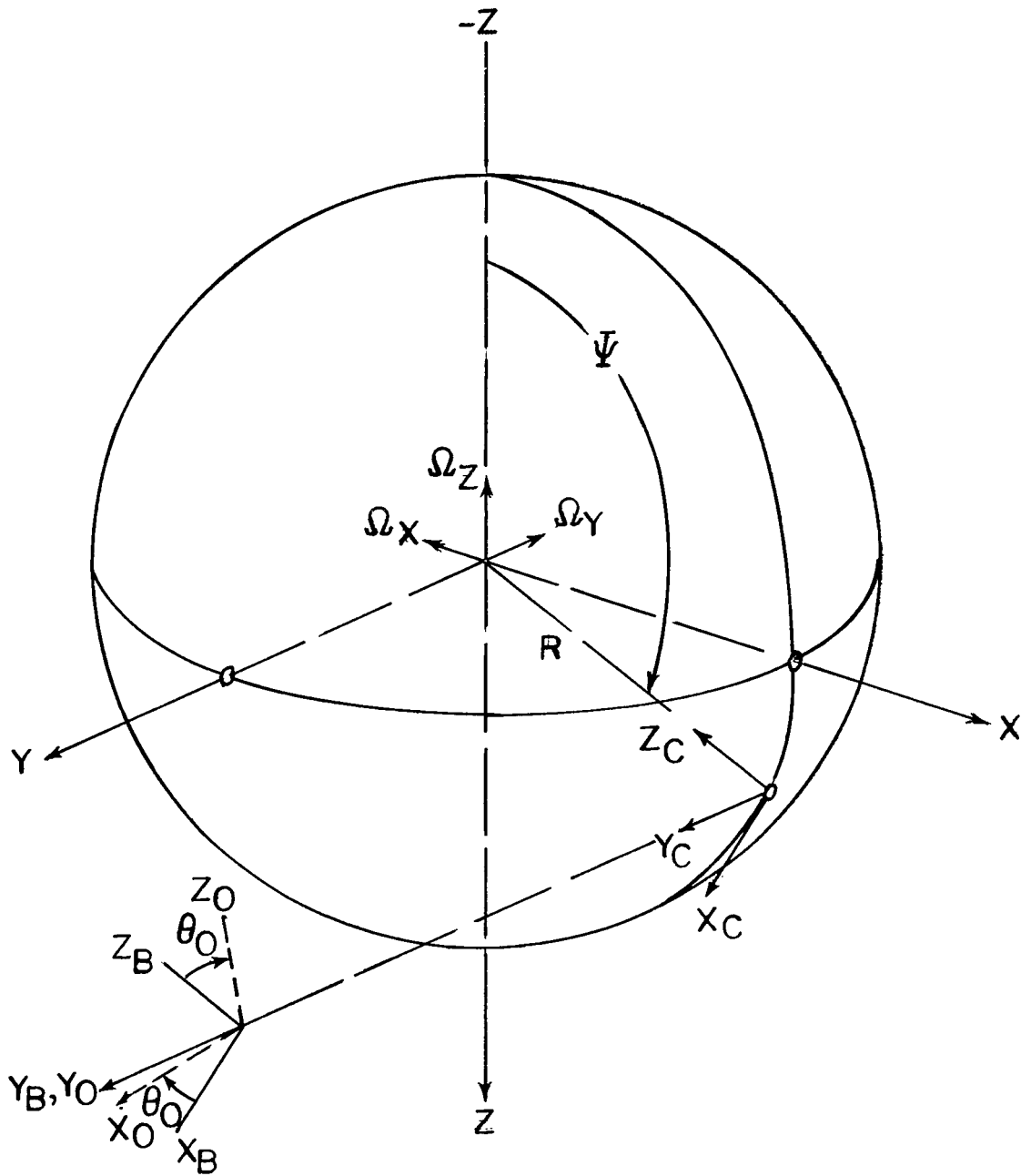
Figure 14.- Assumed axis systems.
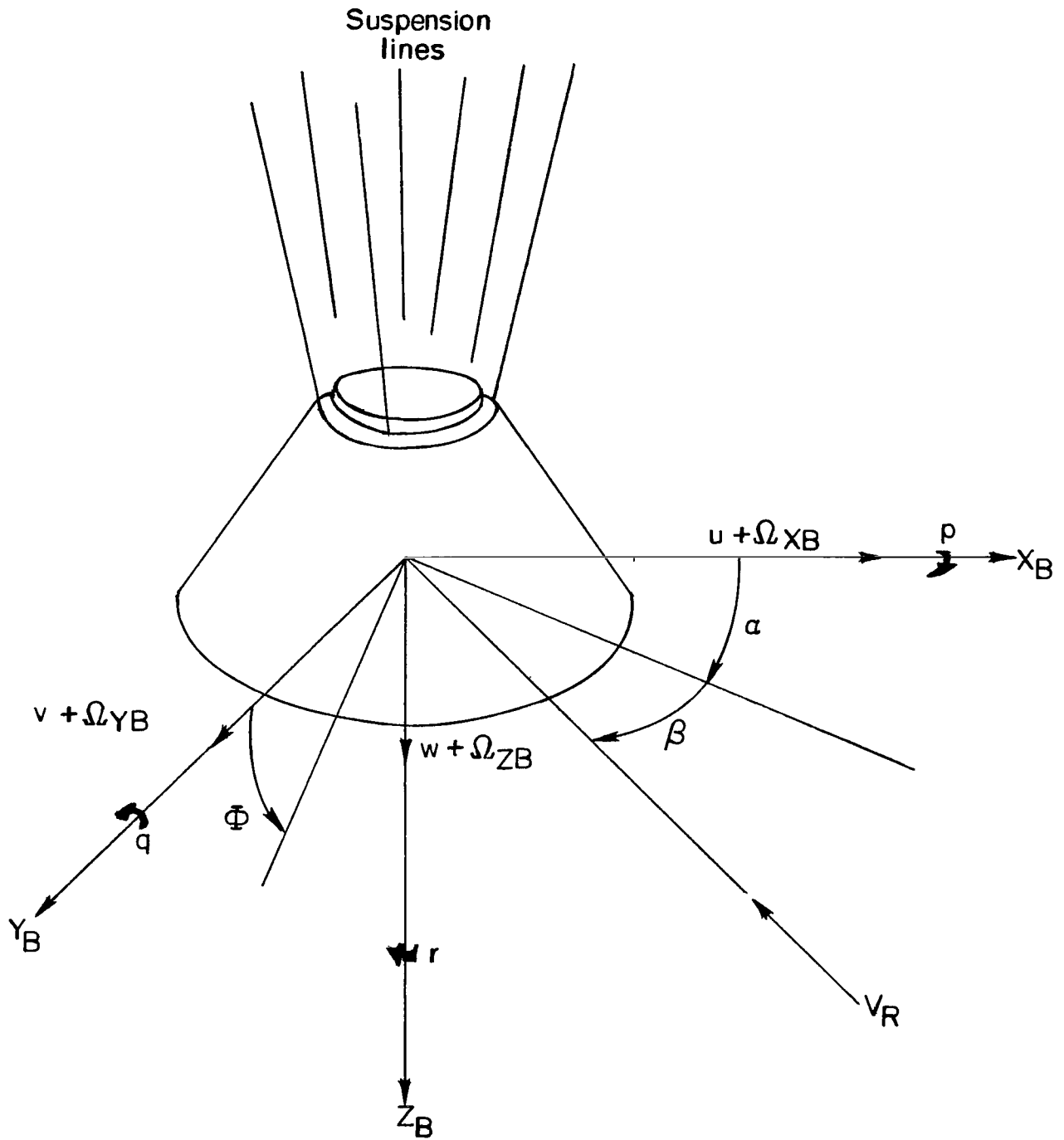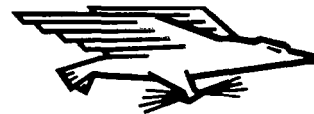
Suspension
lines

$u + \Omega_{XB}$ p X_B

α

$v + \Omega_{YB}$

$w + \Omega_{ZB}$ β

q

Φ

Y_B

r

V_R

Z_B

Figure 14.- Concluded.

"The aeronautical and space activities of the United States shall be conducted so as to contribute . . . to the expansion of human knowledge of phenomena in the atmosphere and space. The Administration shall provide for the widest practicable and appropriate dissemination of information concerning its activities and the results thereof."

— NATIONAL AERONAUTICS AND SPACE ACT OF 1958

NASA SCIENTIFIC AND TECHNICAL PUBLICATIONS

TECHNICAL REPORTS: Scientific and technical information considered important, complete, and a lasting contribution to existing knowledge.

TECHNICAL NOTES: Information less broad in scope but nevertheless of importance as a contribution to existing knowledge.

TECHNICAL MEMORANDUMS: Information receiving limited distribution because of preliminary data, security classification, or other reasons.

CONTRACTOR REPORTS: Scientific and technical information generated under a NASA contract or grant and considered an important contribution to existing knowledge.

TECHNICAL TRANSLATIONS: Information published in a foreign language considered to merit NASA distribution in English.

SPECIAL PUBLICATIONS: Information derived from or of value to NASA activities. Publications include conference proceedings, monographs, data compilations, handbooks, sourcebooks, and special bibliographies.

TECHNOLOGY UTILIZATION PUBLICATIONS: Information on technology used by NASA that may be of particular interest in commercial and other non-aerospace applications. Publications include Tech Briefs, Technology Utilization Reports and Notes, and Technology Surveys.

Details on the availability of these publications may be obtained from:

SCIENTIFIC AND TECHNICAL INFORMATION DIVISION

NATIONAL AERONAUTICS AND SPACE ADMINISTRATION

Washington, D.C. 20546